SCUOLA DI SCIENZE

Dipartimento di Chimica Industriale“Toso Montanari”

Corso di Laurea Magistrale in

Chimica Industriale

Classe LM-71 - Scienze e Tecnologie della Chimica Industriale

Synthesis and Characterization of Atropisomeric Bis-arylboryl-Carbazoles for use in CP-OLEDs

Tesi di laurea sperimentale

CANDIDATO

Claudio Lorenzi

RELATORE

Chiar.mo Prof. Michele Mancinelli

CORRELATORE

Nunzio Matera

Anno Accademico 2022-2023

Abstract:

This work presents the synthesis and characterization of two functionalized atropisomeric amino-boranes. The two products are composed of a boron atom bonded with three different aryl groups: a mesityl substituent, a 2-trifluoromethyl-toluyl substituent and an asymmetrically substituted carbazole moiety. A methacrylate group was installed on the carbazole scaffold with and without an alkyl “spacer” in between. We performed an extensive computational analysis to gather predictions on the energies and peculiar geometries of the ground states, on the energies related to the many transition states that allow stereoisomerization, on the fluorescent and solvatochromic properties and lastly on circularly polarized luminescence.

The synthesis was followed by CSP-HPLC, separating the four atropisomers of each product. The single atropisomers underwent two kinetic studies to experimentally determine the two energy barriers for stereoisomerization. Through Dynamic HPLC we studied the racemization kinetics and via Dynamic NMR the E-Z interconversion kinetics. For each atropisomer we determined the absolute configuration by matching its ECD spectrum with the ones predicted from the computational study (TD-DFT). Fluorescence was visually verified by placing the products under a 366 nm UV light.

Sommario:

In questo progetto viene presentata la sintesi e caratterizzazione di due ammino-borani atropisomerici funzionalizzati. I due prodotti sono formati da un atomo di boro legato a tre gruppi arilici diversi: un sostituente mesitile, un sostituente 2-trifluorometil-toluile e un gruppo carbazolo sostituito asimmetricamente. Un gruppo metacrilato è stato inserito sul carbazolo con e senza uno “spacer” in mezzo. Abbiamo eseguito una ampia analisi computazionale per fare predizioni sulle energie e peculiari geometrie degli stati fondamentali, sulle energie relative ai tanti stati di transizione che permettono la stereoisomerizzazione, sulle proprietà di fluorescenza e solvatocromismo e infine sulla luminescenza circolarmente polarizzata.

Alla sintesi seguì la CSP-HPLC, con cui si separano i quattro atropisomeri di ogni prodotto. I singoli atropisomeri sono stati sottoposti a due studi cinetici per determinare sperimentalmente le due barriere energetiche per la stereoisomerizzazione. Tramite Dinamica HPLC abbiamo studiato le cinetiche di racemizzazione e con Dinamica NMR le cinetiche della interconversione E-Z. Per ogni atropisomero abbiamo determinato la configurazione assoluta confrontando il suo spettro ECD con quelli predetti dagli studi computazionali (TD-DFT). La fluorescenza è stata visivamente confermata mettendo i prodotti sotto una luce UV da 366 nm.

Index:

1. Introduction: **1**
1.1. LEDs: 1
1.2. OLEDs: 1
1.3. 3rd and 4th generation OLEDs: 4
1.4. OLED fabrication: 4
1.5. Aggregation Induced Emission (AIE): 5
1.6. Twisted intramolecular charge transfer (TICT): 5
1.7. DFT and TD-DFT: 6
1.8. Circularly polarized light and ECD: 7
1.9. CP-OLEDs: 8
1.10. Atropisomerism: 8
1.11. Amino-boranes and their photophysical properties: 9
2. Aim of the thesis: **11**
3. Results and discussion: **12**
3.1. Ground states: 12
3.2. Fluorescence: 13
3.3. Transition states: 16
3.4. CSP-HPLC and ECD spectra: 19
3.5. Third barrier kinetics (racemization): 22
3.6. Second barrier kinetics (E-Z interconversion): 24
4. Conclusions: **29**
4.1. Results: 29
4.2. Future prospects: 30
5. Experimental section: **30**
5.1. Instrumentations: 30
5.2. Materials: 31
5.3. Calculations: 31
5.4. Synthesis and NMR characterization: 32
6. Bibliography: **39**

1. Introduction:

1.1. LEDs:

A light-emitting diode, or LED, is a type of *p*-*n* semiconductor diode used to generate light[1].
When a voltage is applied, electrons are inserted into the conduction band of the semiconductor at the cathode and are withdrawn from the valence band at the anode. In other words, electrons are injected at the cathode and electron "holes" are injected at the anode.
Electrons and electron "holes" travel until they meet, releasing energy in the form of photons. This energy relates to the energy gap between the conductive and the valence band of the semiconductor.
LEDs, and *p*-*n* diodes in general, are made of two layers of an inorganic semiconductor doped with specific impurities so that, near the junction (*p*-*n* junction), one layer (*n*-type, rich in mobile electrons) will spontaneously donate some electrons to the other layer (*p*-type, rich in mobile holes), forming two positively/negatively charged regions where there are almost no mobile charges.
These two regions do not allow current to pass through them and are therefore known as the depletion zone. LEDs are diodes because they conduct electricity only in one direction; when the negative electrode (cathode) is correctly placed on the *n*-type layer, the depletion zone shrinks and allows current through.

1.2. OLEDs:

Organic light-emitting diodes, or OLEDs, are organic materials capable of generating light when an electric current is passed through them[2]. They work similarly to LEDs, but they do not have a *p*-*n* junction. The electrons are injected into the LUMOs of the material and withdrawn from the HOMOs, instead of being injected into the conduction band and from the valence band.
Early OLEDs consisted of two layers of organic material sandwiched between anode and cathode. The conductive layer transports holes from the anode and the emissive layer transports electrons from the cathode. Electrons and holes meet at the interface, releasing energy in the form of photons.

Modern OLEDs contain a hole transport layer (HTL) near the anode, an electron transport layer (ETL) near the cathode and an emissive layer where electrons and holes meet. This increases OLED efficiency[3].

When an electron and a hole get close to each other they form an exciton, a neutral and mobile quasiparticle where they are bound together by electrostatic attraction. The exciton is stabilized by resonance stabilization and the repulsive Coulomb forces between the mobile electron and all the electrons surrounding the hole.

In absence of external control[4], electrons and holes have a random spin (+1/2 or -1/2) and the formed exciton can be in a singlet state (S_1), with spin component $m_s = 0$, or in a triplet state (T_1), with spin component $m_s = -1$, 0 or +1 (Figure 1).

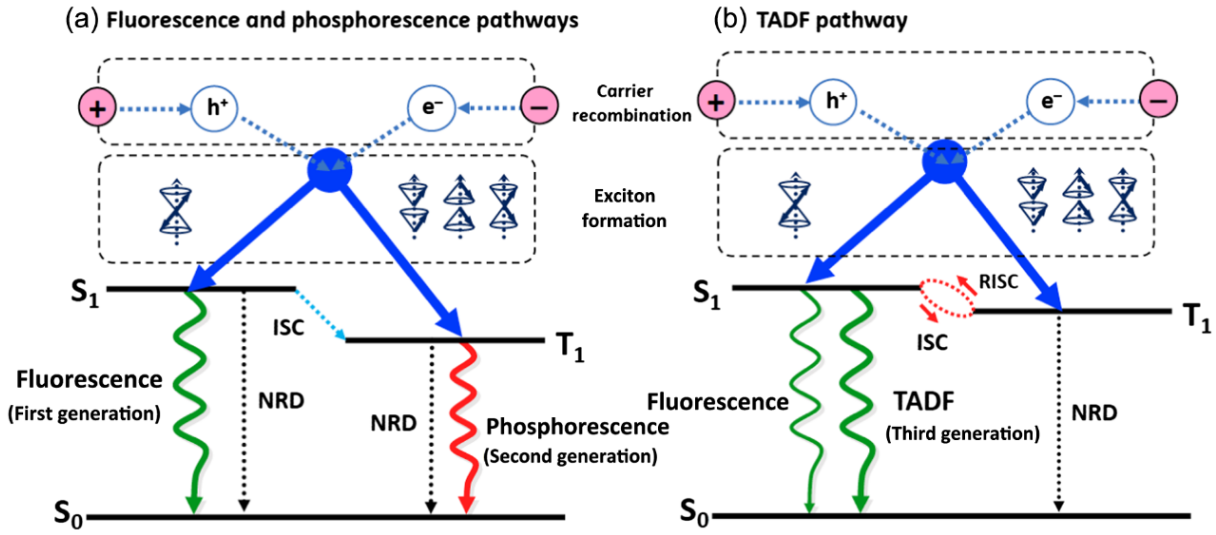

Figure 1: Jablonski diagram and simple pathway illustration for 1st (a), 2nd (a) and 3rd (b) generation OLEDs.

The exciton formed has a 1 in 4 chance of being in a singlet state. In this case the exciton can readily decay, releasing the energy between HOMO (S_0) and LUMO (S_1) as a photon. This event is called fluorescence, and is employed in first generation OLEDs, also known as fluorescent OLEDs (Figure 1a). Because fluorescence can only occur with singlet excitons, the maximum theoretical internal efficiency for fluorescent OLEDs is 25%.

Fluorescent decay is very fast, it takes around 10 ns to occur, but singlet excitons can also undergo nonradiative decay (NRD), through which the energy is released as heat, lowering the internal efficiency of the device. Another unwanted pathway a singlet exciton can take is called intersystem crossing (ISC), which is an isoenergetic process where the singlet excited electron's spin is flipped, changing the system's spin multiplicity and transitioning to a triplet exciton.

After intersystem crossing the newly formed triplet exciton can relax to a slightly lower energy level, losing some energy as heat.

The internal efficiency for first generation OLEDs is capped at 25%, but this limit can be exceeded with Delayed Fluorescence (DF). One example of delayed fluorescence is Triplet-Triplet Annihilation (TTA or TTA-DF), a process where two triplet excitons react to form one singlet exciton[5].

Moreover, the exciton formed has a 3 in 4 chance of being in a triplet state; the radiative decay of triplet excitons is called phosphorescence but it is forbidden by selection rules, therefore it is not readily observed. In fluorescent OLEDs these excitons undergo nonradiative decay, releasing their energy as heat.

Second generation OLEDs, or phosphorescent OLEDs (PHOLEDs), are doped with an organometallic complex that through spin-orbit coupling (SOC) facilitates processes of intersystem crossing and enables room temperature phosphorescence from the lower-lying triplet levels by making use of the heavy-atom effect[6] (Figure 1a). The most common metals used are iridium and platinum (Figure 2), which are very expensive and potentially toxic.

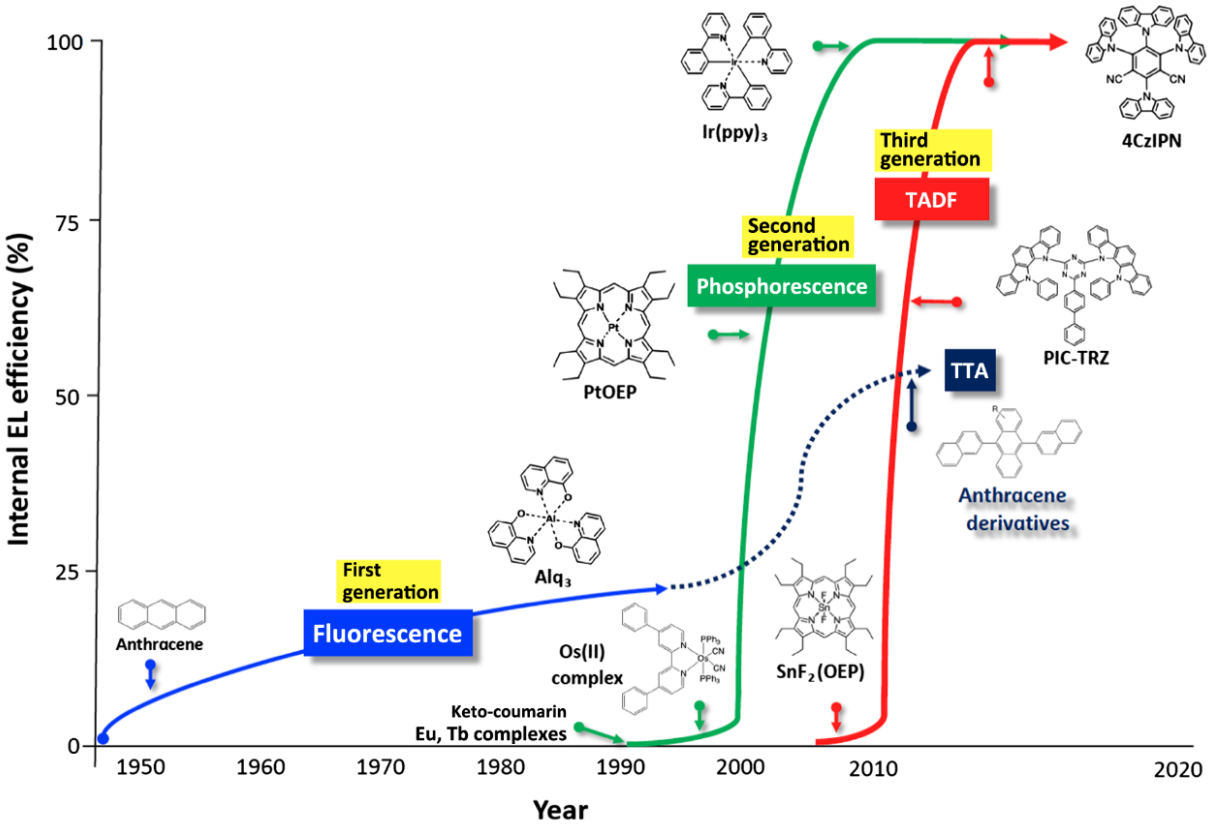

Figure 2: Graph showing the development history for 1st, 2nd and 3rd generation OLEDs, with examples of emitter molecules.

This increase in efficiency is not only important since it reduces energy consumption, but also because it decreases heat generation and, consequently, the air conditioning needed for large displays[7].

1.3. 3rd and 4th generation OLEDs:

Third generation OLEDs contain molecules capable of using thermal energy to convert triplet excitons to singlet excitons through reverse intersystem crossing (RISC), this type of Delayed Fluorescence is called Thermally Activated Delayed Fluorescence (TADF)[8] (Figure 1b). The most important property of TADF materials is the energy gap between triplet and singlet state; the smaller this gap is, the closer it becomes to the average thermal energy of surrounding molecules, speeding up the rate of reverse intersystem crossing.

The most effective strategy for designing TADF molecules with a small T_1-S_1 energy gap is to position electron donating and electron accepting groups spaced apart and twisted each other. This strategy works well because it reduces the geometric differences between triplet and singlet states, which are caused by the spin coupling.

Fourth generation OLEDs use hyperfluorescence to achieve high efficiency. They contain both a TADF molecule and a fluorescent emitter as dopants in a host matrix, and use Förster resonance energy transfer (FRET) to exchange energy between the two[9].

In FRET the energy is transferred through dipole-dipole coupling, so FRET efficiency is inversely proportional to the sixth power of the distance between donor and acceptor.

In fourth generation OLEDs, the two dopants are specifically designed to facilitate FRET from the S_1 state of the TADF molecule to the S_1 state of the fluorescent emitter, while suppressing both ISC on the fluorescent emitter and Dexter electron transfer, which is another energy transfer route[9].

In the absence of strong spin-orbit coupling[10], FRET can only occur between singlet states, while Dexter electron transfer can also happen between triplet states, which is a problem because the T_1 state of the fluorescent emitter can only undergo non-radiative decay.

1.4. OLED fabrication:

Most of the properties of OLED screens and displays are determined by the material used in the emissive layer, it can either be a small molecule in a crystalline phase (small molecule OLEDs or SMOLEDs) or a polymer (polymer OLEDs or POLEDs)[11].

Compared to POLEDs, SMOLEDs have some limitations that complicate their manufacturing process; the poor solubility of the emitting molecules usually means they cannot be fabricated using solution-based processing (spin coating), but instead require the more expensive vacuum vapor deposition[11].

Although the vacuum vapor deposition technique is easier to optimize, SMOLEDs often suffer from limited efficiency and poor stability, due to the formation of unwanted aggregates and due to degradation upon contact with oxygen or water[11]; one way to improve these properties is to encapsulate the small molecule emitter in a polymer[18], this can also make spin coating processes viable since the polymers used are soluble in organic solvents[11]. POLEDs are thus more promising, additionally they have some unique advantages: they can be made flexible and they can operate at a lower voltage[11].

POLEDs can be fabricated through spin coating and inkjet printing; inkjet printing is the method with the greatest potential to minimize production costs, particularly for larger displays.

1.5. Aggregation Induced Emission (AIE):

Many organic luminophores show very different behaviors in dilute and concentrated solutions; for most aromatic hydrocarbons, a rise in concentration or the addition of a non-solvent can cause aggregation-caused quenching (ACQ). As the name suggests, ACQ is the cessation of luminescence due to the formation of aggregates. In many applications, like OLEDs, this is problematic. This problem is often tackled by appending bulky cyclic units to the chromophore or by blending it with a transparent polymer, but both of these approaches reduce OLED efficiency significantly[12].

Luckily, the opposite is true for different compounds that show a very high emission quantum yield only when in solid state or in concentrated solutions. This is known as aggregation-induced emission (AIE)[13].

1.6. Twisted intramolecular charge transfer (TICT):

Twisted intramolecular charge transfer (TICT) is an electron transfer process that occurs in certain molecules after excitation. Molecules that exhibit TICT usually consist of a donor and an acceptor group linked by a single bond, able to twist slightly.

After photoexcitation, the molecule can relax into a locally excited (LE) state, where its geometry isn't much different from that of the ground state. Following, it can also further relax

into a more stable TICT state, redistributing electrons around the nuclei and twisting donor and acceptor groups around the single bond[14] (Figure 3).

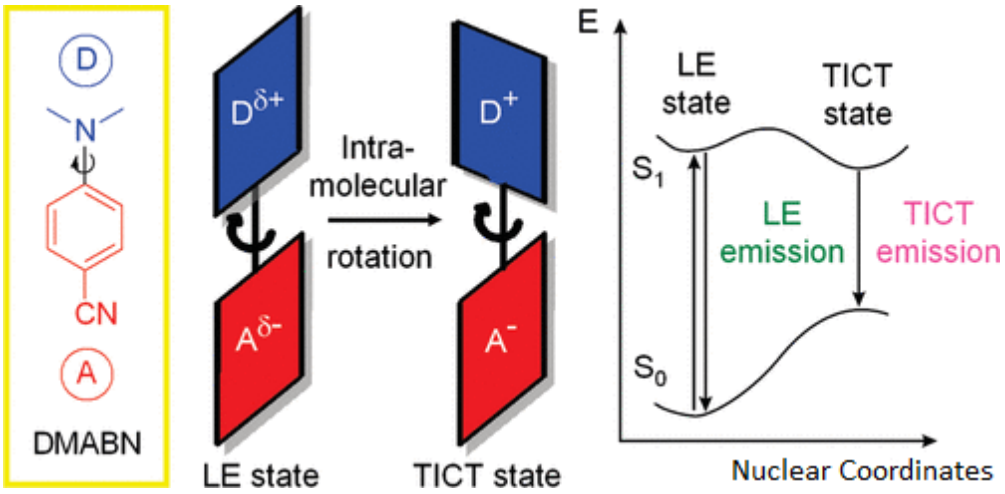

Figure 3: Transition of the locally excited (LE) state of *4-(N,N-dimethylamino)benzonitrile* (DMABN) to the twisted intramolecular charge transfer (TICT) state through intramolecular rotation of its donor (D) and acceptor (A) units at the excited state (S_1).

Since it involves large changes in conformation and dipole moment, this process can be heavily influenced by external factors such as solvent polarity, temperature and pressure[15].

As visually shown in Figure 3, fluorescence emissions from TICT states are lower in energy than the ones from LE states. Because of this, TICT is often related to a strongly redshifted photoemission. The property used to measure this phenomenon is called Stokes shift which is the difference, in wavelength or energy, between the absorption and emission maxima.

Rongrong *et al.* reported strong solvatochromism for DMABM (Figure 3), which is well explained by a TICT mechanism[16].

Solvatochromism is the change in the emission wavelength (color) of a solute based on the solvent it is dissolved in. Polar environments stabilize the TICT state, lowering the S_0-S_1 energy gap and shifting the emission to longer wavelengths (positive solvatochromism or redshift).

1.7. DFT and TD-DFT:

The computational analyses in this work are made using Density-Functional Theory (DFT) and Time-Dependent Density-Functional Theory (TD-DFT).

DFT is a computational methodology used to predict the properties of big molecule and bulk materials on the basis of quantum mechanical considerations. It works by first determining the electron density on the three spatial coordinates (x, y, z) from the potential acting on the

electrons, and then determining the system's properties through functionals of the electron density.

The biggest challenge DFT functionals face is the approximation of the exchange and correlation interactions, which are not exactly known. Hybrid functionals tackle this problem by combining exchange-correlation DFT functionals (based on empirical data or physical constants) with the exact exchange from Hartree-Fock theory. B3LYP is the most used hybrid functional in organic chemistry.

DFT calculations allow us to estimate the geometries and energies of ground states (GS) and transition states (TS), by finding energy minima and first-order saddle points respectively.

Time-dependent DFT (TD-DFT) is an extension of DFT that handles light-matter interactions and other time-dependent processes. In TD-DFT, the time-dependent potential acting on the electrons also depends on the electron density at all previous times.

Through TD-DFT calculations, we can model excited states and predict absorption and emission spectra.

1.8. Circularly polarized light and ECD:

Circularly polarized light is defined as an electromagnetic wave polarized so that its electromagnetic field has a constant magnitude while rotating at a constant rate in a plane perpendicular to its direction. Circularly polarized light can rotate clockwise (right-handed circular polarization, or RHCP) or counter-clockwise (left-handed circular polarization, or LHCP).

A waveplate is a device that alters the polarization state of light, it can be used to produce circularly polarized light and elliptically polarized light from linearly polarized light. Linearly polarized light can be produced with a polarizing filter.

Circular dichroism (CD) of a material is the difference in absorption between left- and right-handed circularly polarized light. Electronic circular dichroism (ECD) is when this absorption occurs in correspondence with electronic transitions, making it the chiroptical counterpart of UV-vis absorption spectroscopy[17].

$$ECD = A_L - A_R$$

ECD is usually measured in *mdeg* units. To quantify this property in a way that is independent from concentration and path length, an analogous of Lambert-Beer law is used:

$$\Delta\epsilon = \epsilon_R - \epsilon_L = \frac{A_L - A_R}{33000 \cdot c \cdot b}$$

Where $\Delta\epsilon$ the difference in molar absorption coefficient ($M^{-1}cm^{-1}$), *c* is the concentration (M) and *b* is the cell path length (cm).

1.9. CP-OLEDs:

Circularly polarized luminescence (CPL) is the direct emission of circularly polarized light, it occurs when the emissive molecule is chiral.

Circularly polarized OLEDs (CP-OLEDs) are a topic of research of great significance; the direct emission of circularly polarized light is central to many applications, including data storage, optical quantum computation, biosensing, environmental monitoring, and display technologies[18].

OLED displays can be made transparent but most displays have one electrode made of ITO (indium tin oxide), which is a very costly transparent material, and one electrode made of cheap, reflective metal[19]. The reflective layer increases the light extraction efficiency of the device, but it also has the detrimental effect of increasing the reflection of the ambient light, decreasing the contrast ratio when the display is used outdoors[20].

Most OLED displays make use of an external antiglare circular polarizer to reduce reflections from other light sources, however this reduces efficiency and performance[21].

CP-OLEDs remove the need for the polarizing filter, simplifying the device's architecture and increasing efficiency[22].

1.10. Atropisomerism:

Atropisomers are stereoisomers that result from hindered rotation around a single bond. This hindrance can be the result of steric obstruction or electronic factors. The rotational energy barrier must be high enough to allow isolation of individual conformers. In 2011, LaPlante *et al.* proposed a simple, qualitative classification of atropisomers[23]:

Class 3: conformers with $\Delta E_{rot} > 30$ kcal/mol have interconversion half-life in the order of years (at 298K), so they can be considered kinetically stable.

Class 2b: conformers with ΔE_{rot} between 23 and 30 kcal/mol can be stored at 298K for hours or weeks.

Class 2a: conformers with ΔE_{rot} between 20 and 23 kcal/mol can be detected and resolved at 298K, but they only last minutes to hours without refrigeration.

Class 1: conformers with $\Delta E_{rot} < 20$ kcal/mol cannot be considered atropisomers at 298K since racemization occurs in the order of nanoseconds to seconds. These conformers must be considered a single entity.

1.11. Amino-boranes and their photophysical properties:

Amino-boranes are cheap and promising compounds, due to their luminescence properties they could find use in many applications, particularly in OLEDs[24], but also in fluorescent probes[25] and in nonlinear optics (NLO)[26].

Many of the properties of amino-boranes arise from the nature of the B-N bond, isoelectronic to a C=C double bond; the filled p_z-orbital of nitrogen next to the empty p_z-orbital of boron forms a stable π-conjugated scaffold with a small HOMO-LUMO gap.

These molecules can also be used in a variety of sensing applications, since they are sensitive to external stimuli such as temperature, pressure and solvents[27].

The molecules shown in Figure 4 have been studied by Paramaguru *et al.* with the aim of developing efficient TADF emitters. They reported that CzBM-1, CzBM-2 and CzBM-3 show notable thermally activated delayed fluorescence (TADF), while CzBM-0 shows no TADF characteristics[28].

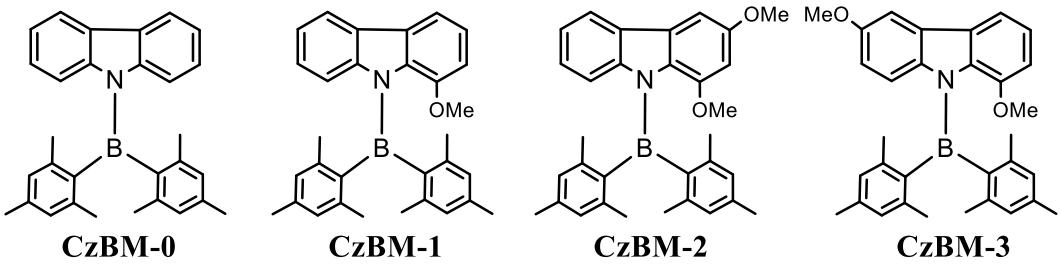

Figure 4: Four molecules studied by Paramaguru *et al.*[28]. The mesityl groups are used because methyl substituents at *orto* positions enhance chemical stability by protecting the boron from nucleophilic attacks.

This is due to the electron donating property and steric encumbrance of the added methoxy group.

In these examples, the carbazole acts as the donating group and $(Mes)_2B$ acts as the acceptor group, so electron-donating substituents on the carbazole or electron-withdrawing substituents on $(Mes)_2B$ enhance the charge transfer (CT) character[29] (Figure 5). Bulky groups also enhance the TICT character because they add steric restrictions, making the B-N bond "pre-twisted"[30].

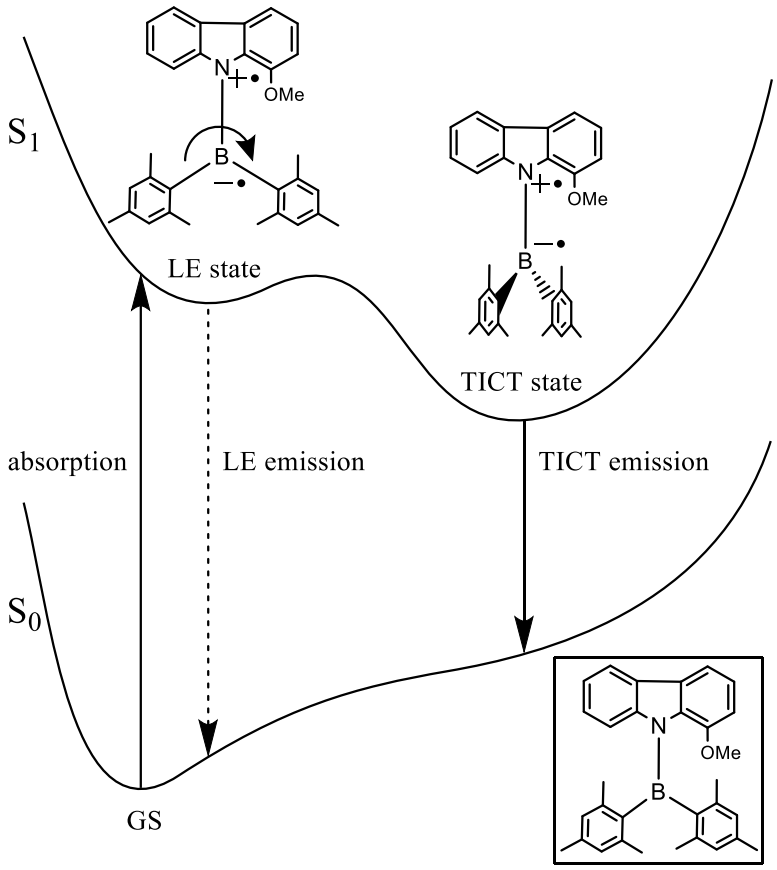

Figure 5: Qualitative energy profile of *9-(dimesitylboraneyl)-1-methoxy-9H-carbazole* over the rotation around the B-N bond, showing ground state (S_0) and excited state (S_1).

TICT and TADF are related because highly pre-twisted donor-acceptor systems minimize the energy gap between singlet (S_1) and triplet (T_1) excitons due to the absence of electron-exchange interactions[30]. So initially populated triplet excitons are rapidly converted to their singlet counterparts on the TICT state, giving the molecule TADF characteristics.
Paramaguru *et al.* also reported strong solvatochromism for CzBM-1, CzBM-2 and CzBM-3[28].

Amino-boranes can show AIE[31], which is crucial in applications like high efficiency OLEDs[13]. Amino-boranes show potential applications in CP-OLEDs since they have all of the characteristics required for creating cheap atropisomeric TADF light-emitting polymers.

2. Aim of the thesis:

The work of this thesis was focused on the synthesis and characterization of a bis-arylboryl-carbazole (product **1**), activated with an electron-donating group on the carbazole:

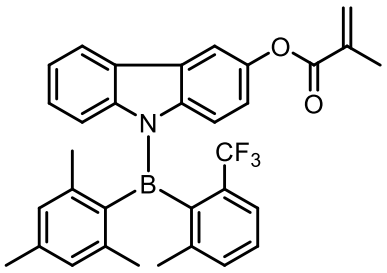

Figure 6: Product **1**, *"9-(mesityl(2-methyl-6-(trifluoromethyl)phenyl)boraneyl)-9H-carbazol-3-yl methacrylate"*

The study of this compound is aimed at developing new host materials for the production of high-efficiency OLED panels and displays.

In particular, it has potential in the development of highly efficient blue TADF emitters[28], which are highly sought after since the ones currently employed suffer from a short lifespan[32].

The methacrylate group is chosen because it makes this molecule a monomer, allowing us to easily incorporate the bis-arylboryl-carbazole into a polymer chain. This compound has two stereogenic axes, so the isolated stereoisomers may show circularly polarized luminescence (CPL) and find applications in CP-OLEDs.

The presence of a polymer chain directly attached to the emitter might favor nonradiative decay (NRD) and compromise its optical properties, considering that the energy of the excited state may readily disperse as vibrational energy in the polymer, instead of being released through fluorescence.

To prevent this, we also designed and synthetized a second compound (product **2**), with a short alkyl chain (a "spacer") to space apart the emitter from the polymer chain:

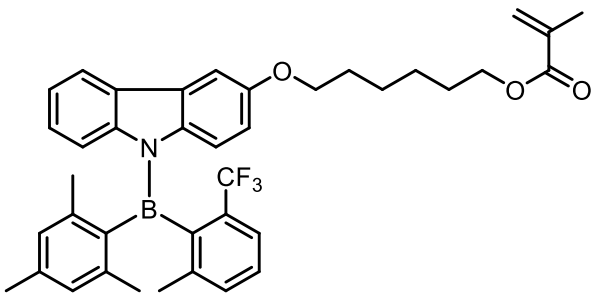

Figure 7: Product **2**, *"6-((9-(mesityl(2-methyl-6-(trifluoromethyl)phenyl)boraneyl)-9H-carbazol-3-yl)oxy)hexyl methacrylate"*

3. Results and discussion:

3.1. Ground states:

Computational DFT analysis gave 8 ground state geometries for product **1** (Table 1).

The stereochemical descriptors used are explained in Figure 8.

Product **1**	GS1	GS2	GS3	GS4	GS5	GS6	GS7	GS8
Configuration	P_A,E, P_H,M_M	P_A,E, P_H,P_M	P_A,E, M_H,M_M	P_A,E, M_H,P_M	P_A,Z, P_H,M_M	P_A,Z, P_H,P_M	P_A,Z, M_H,M_M	P_A,Z, M_H,P_M
ΔG (kcal/mol)	0.489	0.371	0.200	0.000	0.441	0.939	0.394	0.999
Population at 25°C	10.8%	13.1%	17.5%	24.6%	11.7%	5.0%	12.7%	4.6%

Table 1: Ground state geometries for product **1** with configuration, calculated relative free energy and population.

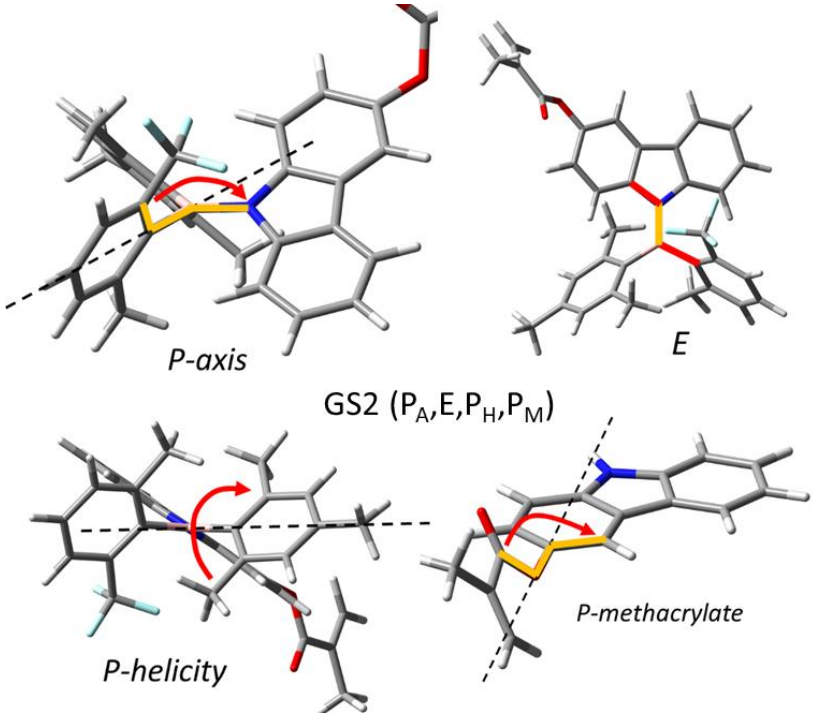

Figure 8: Visual explanation of the stereochemical descriptors used for product **1**, using GS2 as an example.

For the computational DFT analysis of product **2,** an approximation was made: we decided to only perform calculations on a section of the molecule (Figure 9). The alkyl chain and methacrylate group should not affect the electronic properties of the π-conjugated system; they only add unnecessary complexity, which could increase computation time significantly.

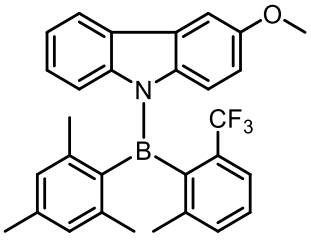

Figure 9: Molecule used for the DFT analysis of product **2**,
"9-(mesityl(2-methyl-6-(trifluoromethyl)phenyl)boraneyl)-3-methoxy-9H-carbazole"

DFT analysis of product **2** showed 4 ground state geometries (Table 2). The stereochemical descriptors used are the same as above.

Product **2**	GS1	GS2	GS3	GS4
Configuration	P_A,Z,M_H	P_A,E,M_H	P_A,Z,P_H	P_A,E,P_H
ΔG (kcal/mol)	0.000	0.277	0.449	0.388
Population at 25°C	38.2%	24.0%	17.9%	19.9%

Table 2: Ground state geometries for product **2** with configuration, calculated relative free energy and population.

3.2. Fluorescence:

Through TD-DFT, we calculated the fluorescence properties of all of these configurations for product **1** (Table 3) and product **2** (Table 4) in three different solvents: tetrahydrofuran (THF), hexane (HEX) and acetonitrile (ACN).

Product **1**	Solvent	Absorption energy (nm)	Emission energy (nm)	Stokes shift (nm)	α (S_0)	α (S_1)	|Δα|
GS1	THF	296.413	490.793	194.380	-149.21	-120.69	28.52
	HEX	300.436	467.494	167.057	-150.30	-119.29	31.01
	ACN	294.207	500.416	206.209	-148.76	-121.12	27.64
GS2	THF	296.065	488.793	192.728	-149.58	-120.63	28.95
	HEX	300.926	466.518	165.592	-150.22	-118.98	31.24
	ACN	293.627	498.230	204.604	-149.04	-121.26	27.78
GS3	THF	297.017	484.973	187.956	143.29	120.37	22.92
	HEX	300.341	444.225	143.884	143.33	119.44	23.89
	ACN	295.603	503.476	207.873	143.22	120.74	22.48
GS4	THF	297.811	485.503	187.692	142.91	120.54	22.37
	HEX	300.161	444.662	144.502	142.60	119.54	23.06
	ACN	295.922	505.403	209.481	143.12	120.72	22.40
GS5	THF	296.297	491.583	195.287	30.30	59.92	29.62
	HEX	301.178	466.343	165.165	29.93	61.35	31.42
	ACN	293.998	501.420	207.422	30.62	59.32	28.70
GS6	THF	296.734	489.042	192.309	30.36	59.84	29.48
	HEX	301.374	464.279	162.906	29.64	61.34	31.70
	ACN	293.832	498.094	204.261	30.52	59.16	28.64
GS7	THF	297.554	482.227	184.673	-30.55	-58.79	28.24
	HEX	299.434	442.302	142.868	-29.91	-60.21	30.30
	ACN	296.244	501.597	205.353	-30.86	-58.36	27.50
GS8	THF	297.410	484.698	187.288	-30.79	-58.85	28.06
	HEX	300.079	444.327	144.249	-30.30	-60.07	29.77
	ACN	295.677	503.666	207.989	-31.22	-58.79	27.57

Table 3: Calculated fluorescence properties of product **1**.

Product **2**	Solvent	Absorption energy (nm)	Emission energy (nm)	Stokes shift (nm)	α (S_0)	α (S_1)	|Δα|
GS1	THF	310.379	575.190	264.811	-29.89	-60.49	30.60
	HEX	311.826	496.558	184.732	-29.52	-61.89	32.37
	ACN	308.075	615.501	307.426	-30.02	-60.14	30.12
GS2	THF	311.710	580.246	268.536	144.14	119.71	24.43
	HEX	313.921	503.415	189.494	144.10	118.62	25.48
	ACN	309.197	620.074	310.877	144.09	120.13	23.96
GS3	THF	309.643	590.273	280.630	29.26	60.43	31.17
	HEX	315.308	531.628	216.319	28.74	61.76	33.02
	ACN	305.619	617.959	312.340	29.48	60.03	30.55
GS4	THF	308.155	581.910	273.755	-150.51	-119.36	31.15
	HEX	313.886	532.996	219.110	-151.15	-117.62	33.53
	ACN	304.167	604.377	300.210	-150.14	-119.94	30.20

Table 4: Calculated fluorescence properties of product **2.**

The angle α, listed in Tables 3 and 4, is the dihedral angle shown in Figure 10.

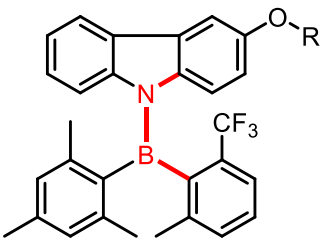

Figure 10: Highlighted are the four atoms that form the dihedral angle α.

These results show for both products a notable solvatochromic effect; across all ground states, a polar solvent like acetonitrile leads to higher Stokes shifts while an apolar solvent like hexane leads to lower Stokes shifts.

We can also see a very large change in the dihedral angle on the B-N bond between ground state (S_0) and excited state (S_1). The difference in the dihedral angle is affected by the solvent as well; apolar solvents lead to slightly greater change in the dihedral angle.

These very large stoke shifts, together with the solvatochromic effect and the sizable changes in the dihedral angle, indicate that these molecules undergo twisted intramolecular charge transfer (TICT). This can be further verified by looking at the rendering of frontier molecular orbitals:

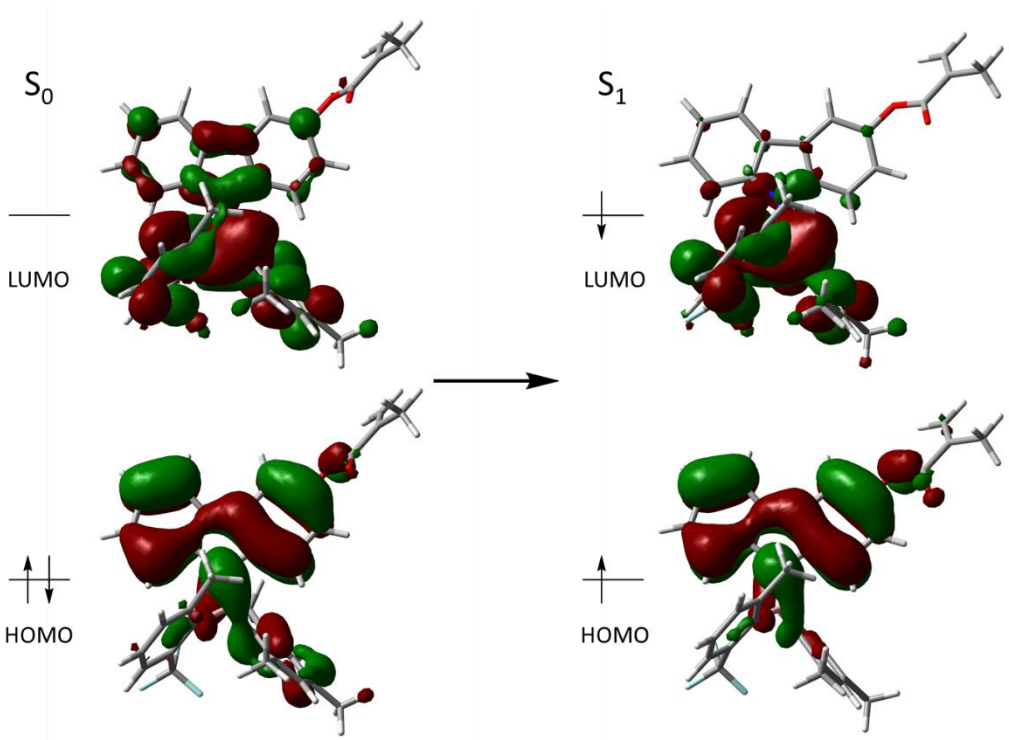

Figure 11: Renderings of frontier molecular orbitals for product **1**, the configuration shown is GS4 (P_A,E,M_H,P_M) in THF. GS4 is chosen because it is the most populated, but all configurations reveal the same general shapes.

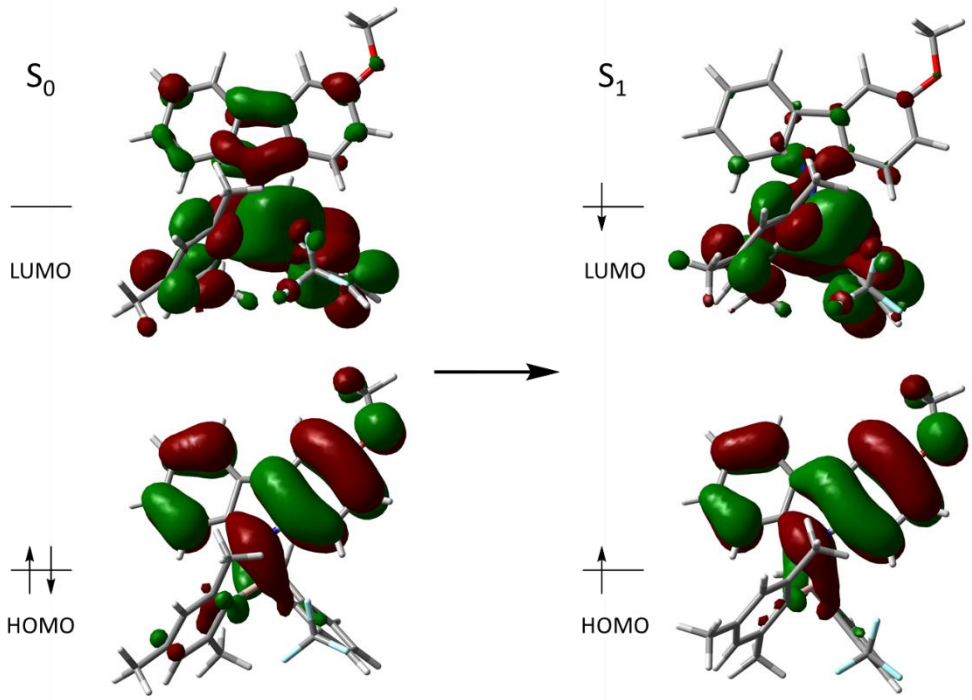

Figure 12: Renderings of frontier molecular orbitals for product **2**, the configuration shown is GS1 (P_A,Z,M_H) in THF. GS1 is chosen because it is the most populated, but all configurations reveal the same general shapes.

From Figures 11 and 12, we can clearly see that for both products the calculated HOMO and LUMO at the ground state (S_0) generally reside in different parts of the molecule: the HOMO is mainly located on the carbazole, which is the donor group of the intramolecular charge transfer, while the LUMO is mainly on $(Aryl)_2B$, which is the acceptor group.

This difference in electron distribution gets more extreme after relaxation on the excited state (S_1). This is consistent with the TICT model.

Products **1** and **2** display the same general behavior but they also show some differences; from Figures 3 and 4, we can see that product **2** has greater stoke shifts and changes in the dihedral angle, this is indicative of a stronger TICT character.

This can be explained by looking at the electronic properties of the substituent groups added to the carbazole; product **2** has an ether group, which is electron-donating, while product **1** has a methacrylate group, which is much less electron-donating.

An electron-donating substituent on the carbazole, which is the donor group of the charge transfer, should stabilize the excited state (S_1) and promote the TICT. This should result in higher stoke shifts and greater changes in geometry, which is exactly what we see.

3.3. Transition states:

The only feasible mechanism for the stereoisomerization of products **1** and **2** is the torsional motion around the B-N bond and around the two B-C bonds[33]; these molecules are propeller-like in shape and the motions of the three aromatic rings are geared together.[34] Considering the reference plane CB-NC, for every ring, transition states involve passage through either the reference plane or a plane perpendicular to the reference plane.

In this work we will be using the "ring flip" nomenclature proposed by Mislow for tris-aryl boranes[33,34], which labels transition states based on the number of rings that pass through a plane perpendicular to the reference plane (these rings are said to "flip").

In Figure 13, we can see all eight possible transition states:

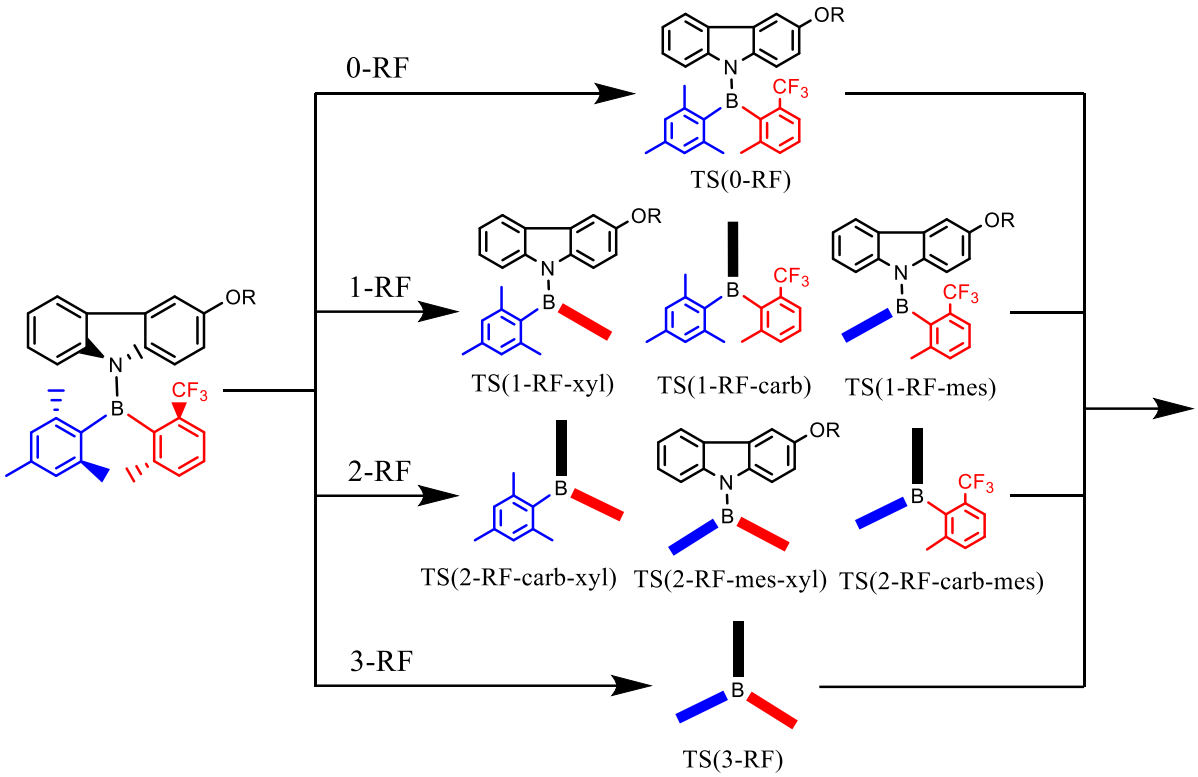

Figure 13: All possible transition states for products **1** and **2**, labelled with Mislow's ring flip (RF) nomenclature. The rectangles represent the aryl groups (according to their colour) that are perpendicular to the reference plane.

The only stereoisomerization mechanism of practical concern is the two-ring flip (2-RF), since it is the one with the lowest energy[34,33].

We performed DFT analysis to get an estimate of the energy barriers associated with the three types of transition state:

Transition state type	Name	ΔG (kcal/mol)	Relative ΔG (kcal/mol)	Stereoisomerization reactions
2-RF-carb-mes	TS1	32.661	0.709	GS6P(P_A,Z,P_H,P_M) ⇄ GS1M(M_A,E,M_H,P_M), GS2P(P_A,E,P_H,P_M) ⇄ GS5M(M_A,Z,M_H,P_M)
	TS2	32.102	0.149	GS3M(M_A,E,P_H,P_M) ⇄ GS8P(P_A,Z,M_H,P_M), GS7M(M_A,Z,P_H,P_M) ⇄ GS4P(P_A,E,M_H,P_M)
	TS3	32.142	0.190	GS5P(P_A,Z,P_H,M_M) ⇄ GS2M(M_A,E,M_H,M_M), GS1P(P_A,E,P_H,M_M) ⇄ GS6M(M_A,Z,M_H,M_M)
	TS4	**31.952**	0.000	GS4M(M_A,E,P_H,M_M) ⇄ GS7P(P_A,Z,M_H,M_M), GS8M(M_A,Z,P_H,M_M) ⇄ GS3P(P_A,E,M_H,M_M)
2-RF-carb-xyl	TS5	23.664	0.240	GS2P(P_A,E,P_H,P_M) ⇄ GS8P(P_A,Z,M_H,P_M), GS7M(M_A,Z,P_H,P_M) ⇄ GS1M(M_A,E,M_H,P_M)
	TS6	**23.423**	0.000	GS6P(P_A,Z,P_H,P_M) ⇄ GS4P(P_A,E,M_H,P_M), GS3M(M_A,E,P_H,P_M) ⇄ GS5M(M_A,Z,M_H,P_M)
	TS7	23.691	0.268	GS1P(P_A,E,P_H,M_M) ⇄ GS7P(P_A,Z,M_H,M_M), GS8M(M_A,Z,P_H,M_M) ⇄ GS2M(M_A,E,M_H,M_M)
	TS8	23.452	0.029	GS5P(P_A,Z,P_H,M_M) ⇄ GS3P(P_A,E,M_H,M_M), GS4M(M_A,E,P_H,M_M) ⇄ GS6M(M_A,Z,M_H,M_M)

2-RF-mes-xyl	TS9	13.373	0.102	GS3M(M_A,E,P_H,P_M) ⇄ GS1M(M_A,E,M_H,P_M), GS2P(P_A,E,P_H,P_M) ⇄ GS4P(P_A,E,M_H,P_M)
	TS10	13.753	0.482	GS6P(P_A,Z,P_H,P_M) ⇄ GS8P(P_A,Z,M_H,P_M), GS7M(M_A,Z,P_H,P_M) ⇄ GS5M(M_A,Z,M_H,P_M)
	TS11	**13.271**	0.000	GS4M(M_A,E,P_H,M_M) ⇄ GS2M(M_A,E,M_H,M_M), GS1P(P_A,E,P_H,M_M) ⇄ GS3P(P_A,E,M_H,M_M)
	TS12	13.330	0.058	GS5P(P_A,Z,P_H,M_M) ⇄ GS7P(P_A,Z,M_H,M_M), GS8M(M_A,Z,P_H,M_M) ⇄ GS6M(M_A,Z,M_H,M_M)
Methacrylate rotation	/	1.804	/	GS1P ⇄ GS2P, GS1M ⇄ GS2M, GS3P ⇄ GS4P, GS3M ⇄ GS4M, GS5P ⇄ GS6P, GS5M ⇄ GS6M, GS7P ⇄ GS8P, GS7M ⇄ GS8M

Table 5: Transition states of product **1**, with their calculated energy barriers and the equilibrium involving them. The methacrylate rotation has an energy barrier of around 2 kcal/mol, it is included only for completeness.

On Table 5, we can see the energy barriers linked to the stereoisomerization of product **1**. The lowest barrier is the one related to the *2-RF-mes-xyl* transition states and is 13.3 kcal/mol. We can see that this transition state only inverts the molecule's helicity, leaving every other stereochemical descriptor unchanged.

The second barrier is related to the *2-RF-carb-xyl* transition and is 23.4 kcal/mol, which is high enough to separate the corresponding diastereoisomers through CSP-HPLC at room temperature and keep them stable with refrigeration. This type of transition state changes both the helicity and the E-Z configuration, so this barrier represents the π-barrier and unlocks the E-Z interconversion.

The third barrier is at 32 kcal/mol and is related to the *2-RF-carb-mes* transition. This type of transition state inverts the axial chirality, the E-Z configuration and the helicity, so this barrier unlocks the inversion of the trifluoro-xylyl chiral axis (P_A to M_A). Starting from E-Z equilibrate mixture, this stereoisomerization can be represented as the racemization inversion. The two pairs of diastereoisomers (E+Z, P_A or M_A) are stable at room temperature.

Transition state type	Name	ΔG (kcal/mol)	Relative ΔG (kcal/mol)	Stereoisomerization reactions
2-RF-carb-mes	TS1	**32.287**	0.000	GS2M(M_A,E,P_H) ⇄ GS1P(P_A,Z,M_H), GS1M(M_A,Z,P_H) ⇄ GS2P(P_A,E,M_H)
	TS2	32.835	0.548	GS3P(P_A,Z,P_H) ⇄ GS4M(M_A,E,M_H), GS4P(P_A,E,P_H) ⇄ GS3M(M_A,Z,M_H)
2-RF-carb-xyl	TS3	**23.774**	0.000	GS4P(P_A,E,P_H) ⇄ GS1P(P_A,Z,M_H), GS1M(M_A,Z,P_H) ⇄ GS4M(M_A,E,M_H)
	TS4	24.329	0.555	GS3P(P_A,Z,P_H) ⇄ GS2P(P_A,E,M_H), GS2M(M_A,E,P_H) ⇄ GS3M(M_A,Z,M_H)
2-RF-mes-xyl	TS5	**12.539**	0.000	GS4P(P_A,E,P_H) ⇄ GS2P(P_A,E,M_H), GS2M(M_A,E,P_H) ⇄ GS4M(M_A,E,M_H)
	TS6	12.634	0.095	GS3P(P_A,Z,P_H) ⇄ GS1P(P_A,Z,M_H), GS1M(M_A,Z,P_H) ⇄ GS3M(M_A,Z,M_H)

Table 6: Transition states of product **2**, with their calculated energies and the reactions involving them.

The computational analysis of product **2** (Table 6) gave similar results. The first barrier is at 12.5 kcal/mol and unlocks the inversion of helicity, the second is at 23.8 kcal/mol and unlocks the E-Z interconversion, the third is at 32.3 kcal/mol and unlocks the inversion of the trifluoro-xylyl chiral axis (P_A to M_A).

3.4. CSP-HPLC and ECD spectra:

CSP-HPLC separation yielded four peaks for both products:

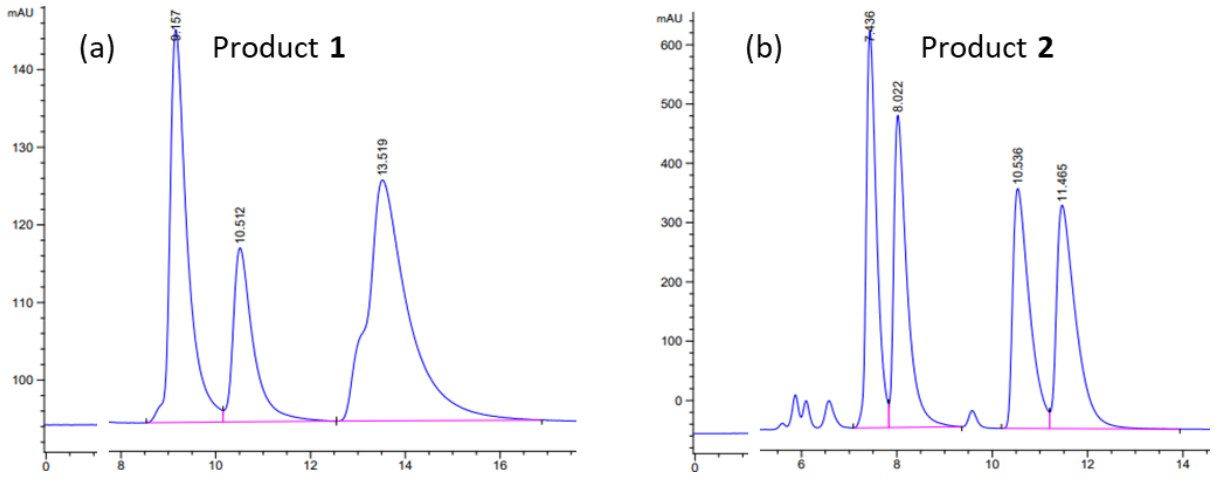

Figure 14: CSP-HPLC spectra of products **1** and **2**.

Product **1** gave an unfortunate chromatogram (Figure 14a): the third and fourth peaks are overlapped, they can be separated neatly only at very small concentrations. Additionally, it shows a very uneven diastereomeric distribution, this seems to be the result of a chiral

precipitation, rather than being its natural equilibrium distribution. This hypothesis was confirmed by a simple experiment explained later (Figure 21).

Product **2** gave a much better spectrum (Figure 14b), although the sample is not very clean, the four enantiomers have been separated efficiently.

To assign the configuration of the trifluoro-xylyl chiral axis (P_A/M_A) to each eluted peak we performed TD-DFT ECD calculations with different functionals and compared them to the experimental ECD spectra we acquired for each eluted sample.

On figure 15, we see the results for product **1**: the first and second peaks have M_A configuration, while the third and fourth have P_A configuration.

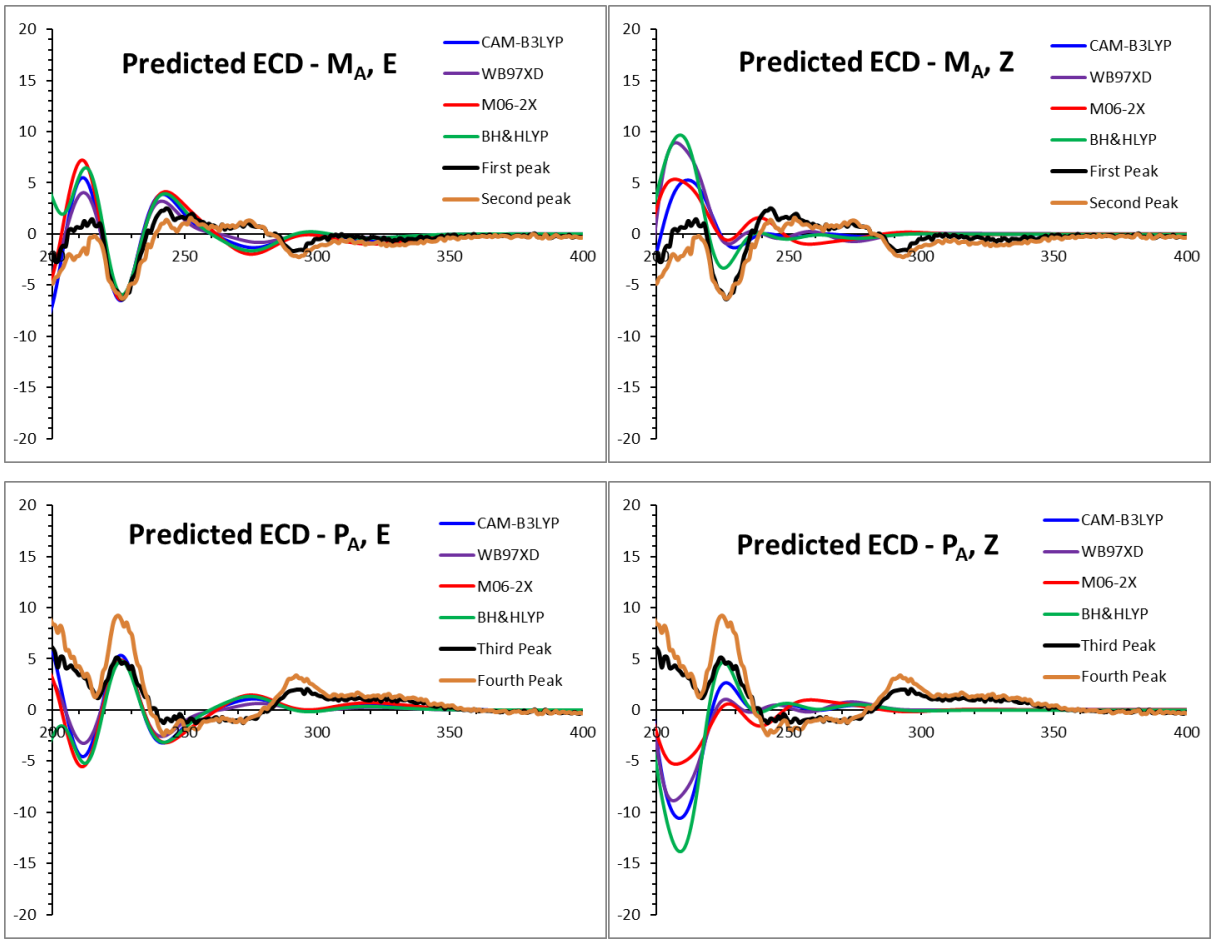

Figure 15: Calculated ECD spectrum for each atropisomer of product **1**, compared to the two similar eluted peaks. The predicted spectra are the weighted sum of the calculated spectra for the concerned ground state geometries.

On Figure 16, we see the results for product **2**: the first and fourth peaks have M_A configuration, while the second and third have P_A configuration.

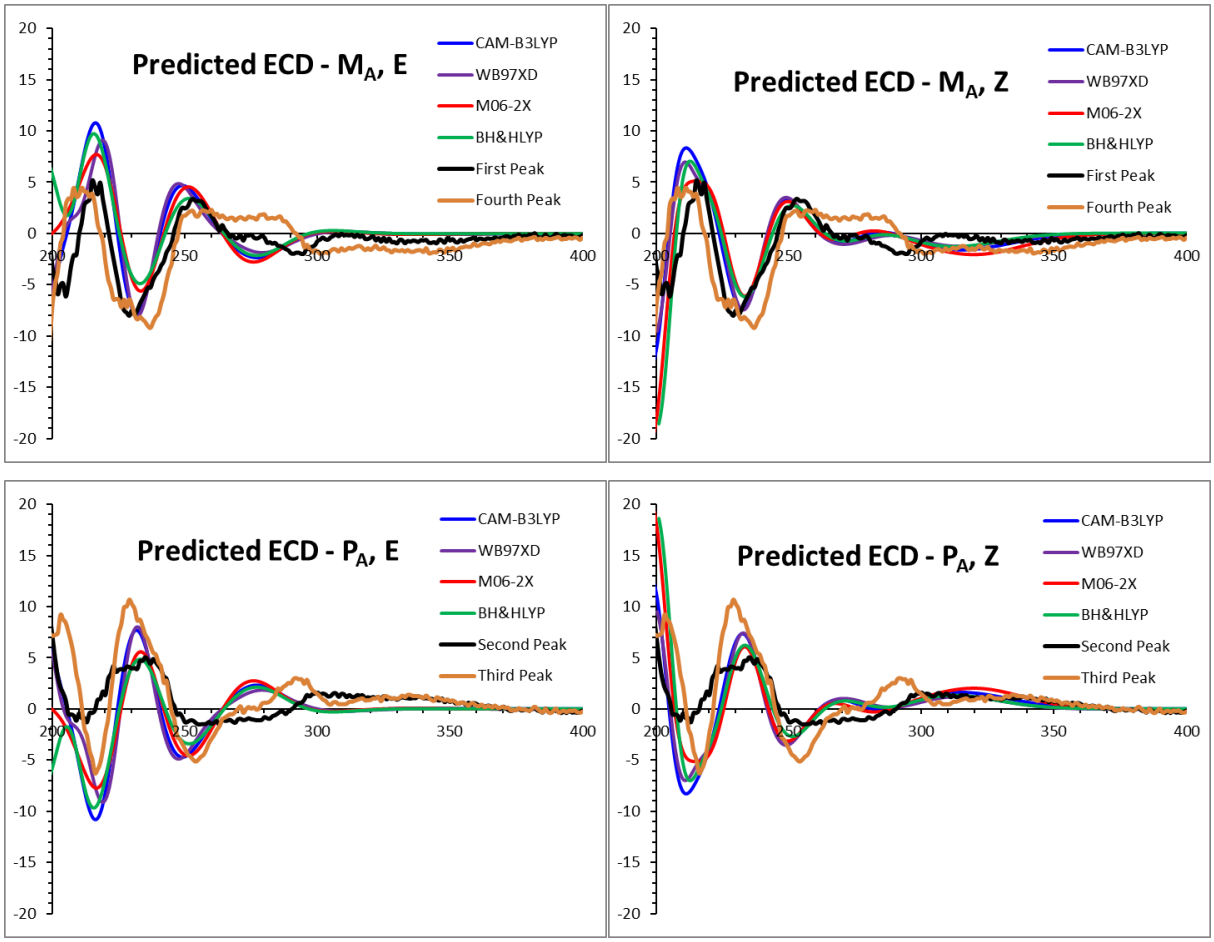

Figure 16: Calculated ECD spectrum for each atropisomer of product **2**, compared to the two similar eluted peaks. The predicted spectra are the weighted sum of the calculated spectra for the concerned ground state geometries.

These results are further confirmed through analysis of a sample from a single peak after partial or total E-Z interconversion. After one or two days at room temperature, we performed CSP-HPLC analysis on a sample from the 1st eluted peak of product **1**, the resulting spectrum showed the 1st and 2nd peak. The same analysis on a sample from the 3rd eluted peak of product **2** showed the 2nd and 3rd peak, and the same analysis on a sample from the 4th eluted peak of product **2** showed the 1st and 4th peak. This is all consistent with the TD-DFT ECD predictions.

To assign the E/Z configuration, NOESY experiments will be performed in future research.

3.5. Third barrier kinetics (racemization):

To experimentally determine the racemization energy barrier, we heated up a sample of a single pair of diastereoisomers (E+Z) diluted in 1,1,2,2-tetrachloroethane and we periodically collected samples that we later analyzed with CSP-HPLC.

For the kinetic analysis of product 1, we took the P_A enantiomer (3^{rd} and 4^{th} peak) and heated it to 120 °C, then we sampled it every 30 min (Figure 17).

Through standard kinetics we can calculate an experimental energy barrier of 32.43 kcal/mol, which is compatible with the previously calculated DFT value of 31.95 kcal/mol (Table 5).

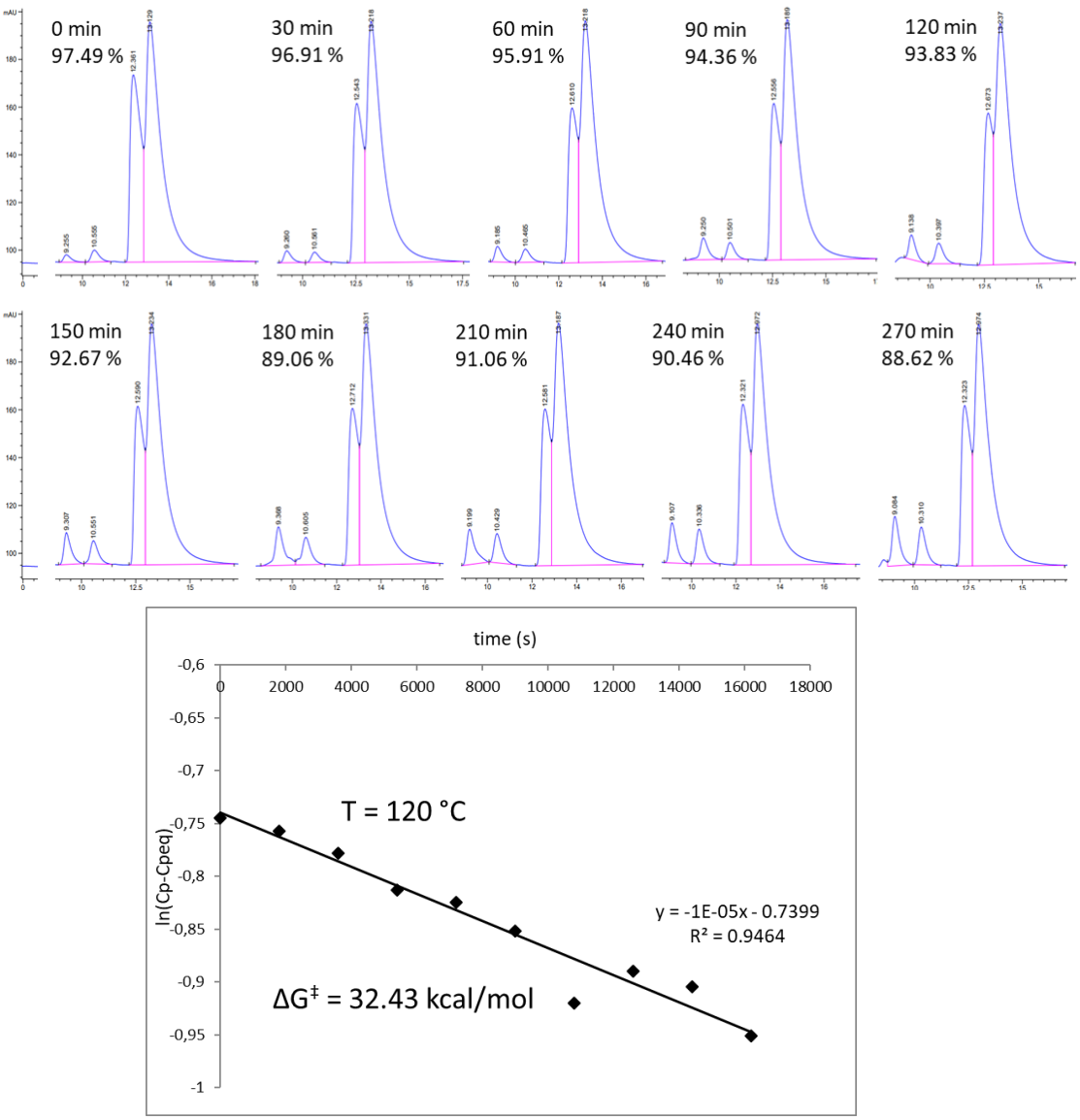

Figure 17: (above) HPLC spectra of the samples periodically taken from the heated P_A enantiomer of product **1**, labelled with the time of sampling and the ratio between the areas of the peaks expressed as a percentage (3^{rd}+4^{th}/1^{st}+2^{nd}). (below) A graph showing the linear regression of the results.

For the kinetic analysis of product **2**, we took the P_A enantiomer (2^{nd} and 3^{rd} peak) and heated it to 130 °C, then we sampled it every 30 min (Figure 18).

The experimental energy barrier is 33.04 kcal/mol, which is compatible with the previously calculated DFT value of 32.29 kcal/mol (Table 6).

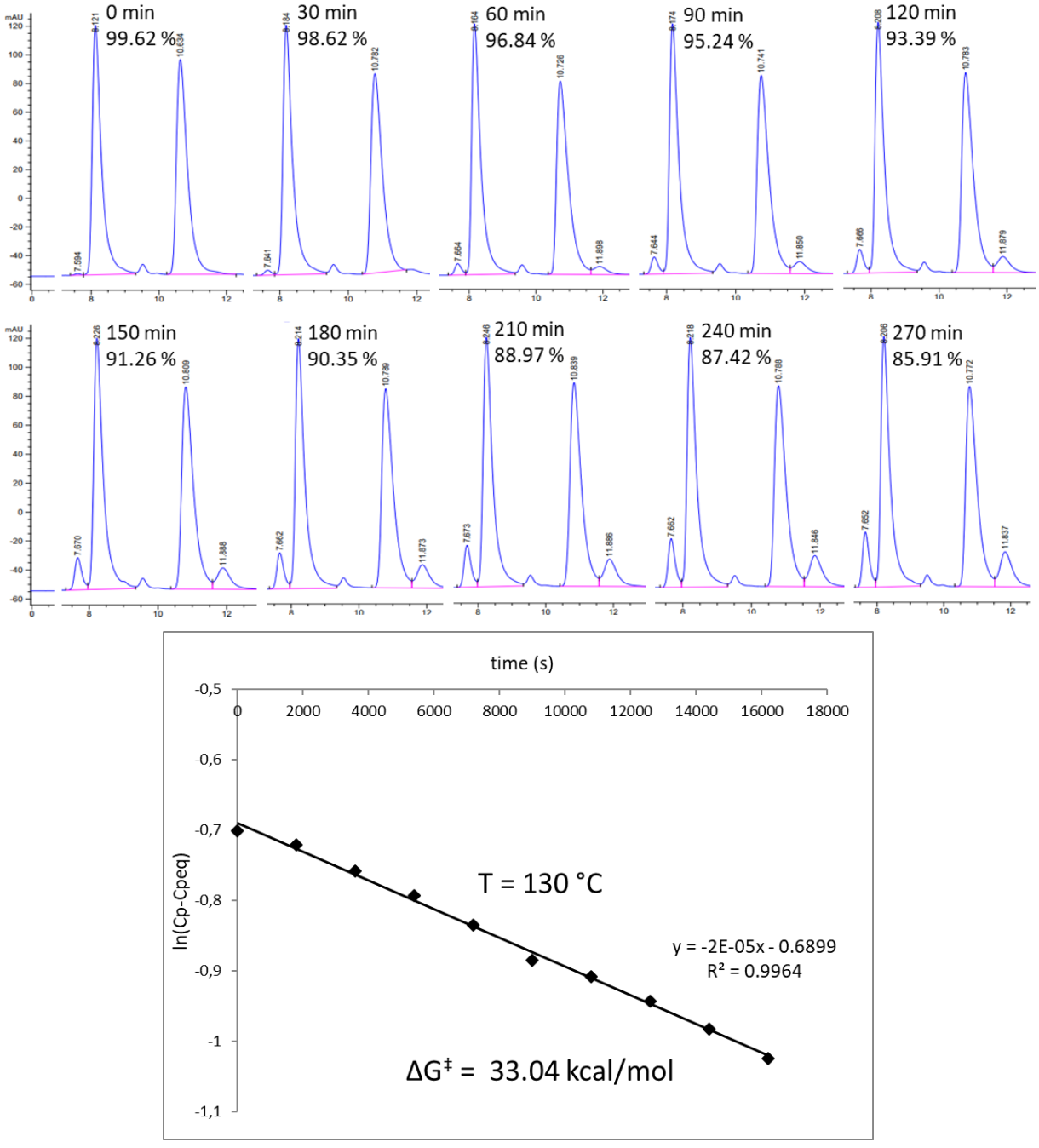

Figure 18: (above) HPLC spectra of the samples periodically taken from the heated P_A enantiomer of product **2**, labelled with the time of sampling and the ratio between the areas of the first two peaks expressed as a percentage ($2^{nd}/1^{st}$), we only used the first two peaks because the 3^{rd} and 4^{th} peaks are overlapping much more. (below) A graph showing the linear regression of the results.

3.6. Second barrier kinetics (E-Z interconversion):

To experimentally determine the E-Z interconversion energy barrier we periodically analyzed a sample from a single eluted peak through NMR spectroscopy, in $CDCl_3$, while keeping it heated to a chosen temperature.

The kinetic analysis of product 1 (Figures 19 and 20) resulted in an experimental energy barrier of 24.9 kcal/mol from the 1st eluted peak and 24.7 kcal/mol from the 2nd eluted peak, which are compatible with the previously calculated DFT value of 23.4 kcal/mol (Table 5).

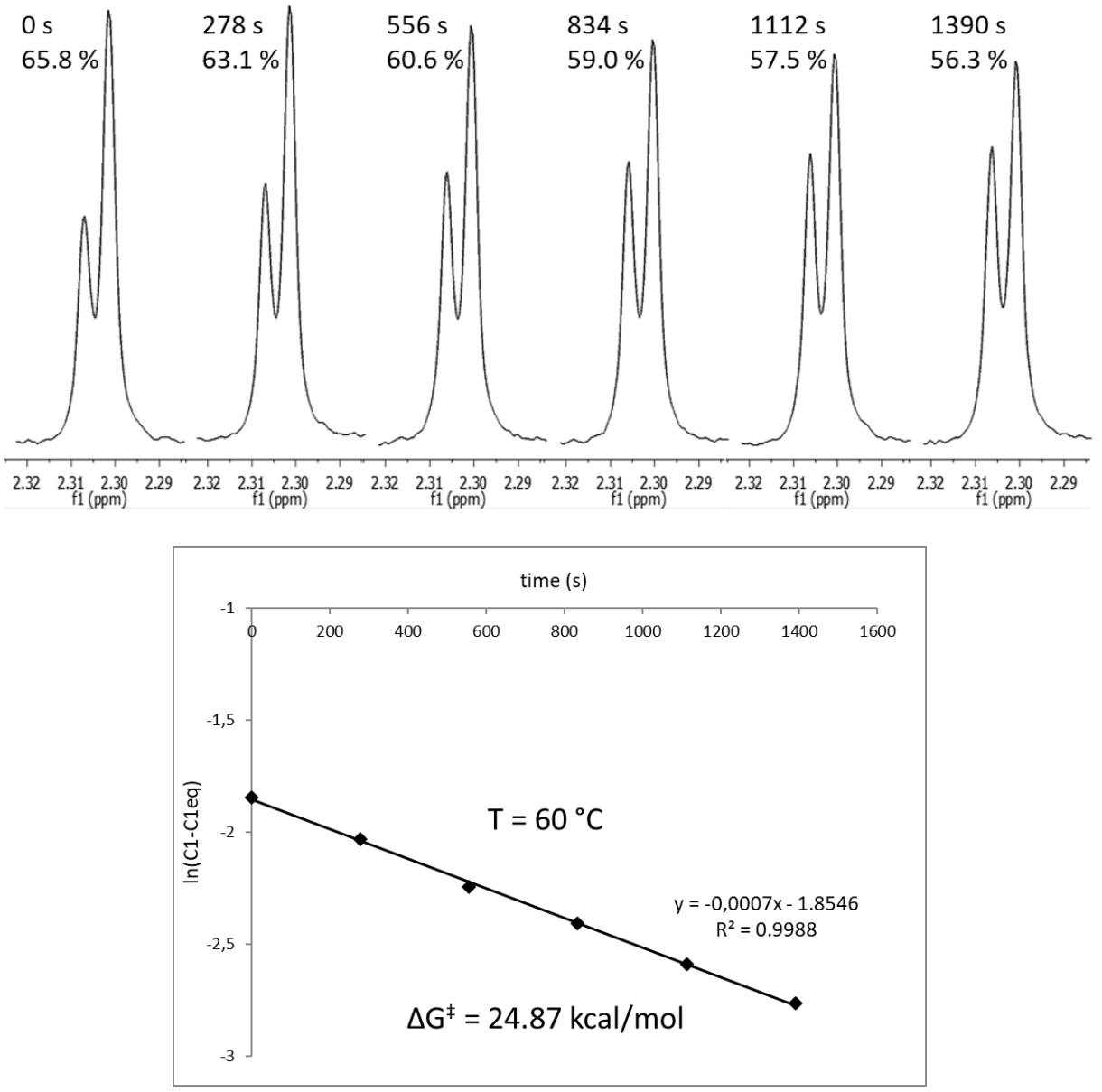

Figure 19: (above) NMR spectra of a sample of the first eluted peak of product **1** taken at intervals of 278 s, labelled with the time waited and the ratio between the heights of the chosen peaks expressed as a percentage. (below) A graph showing the linear regression of the results.

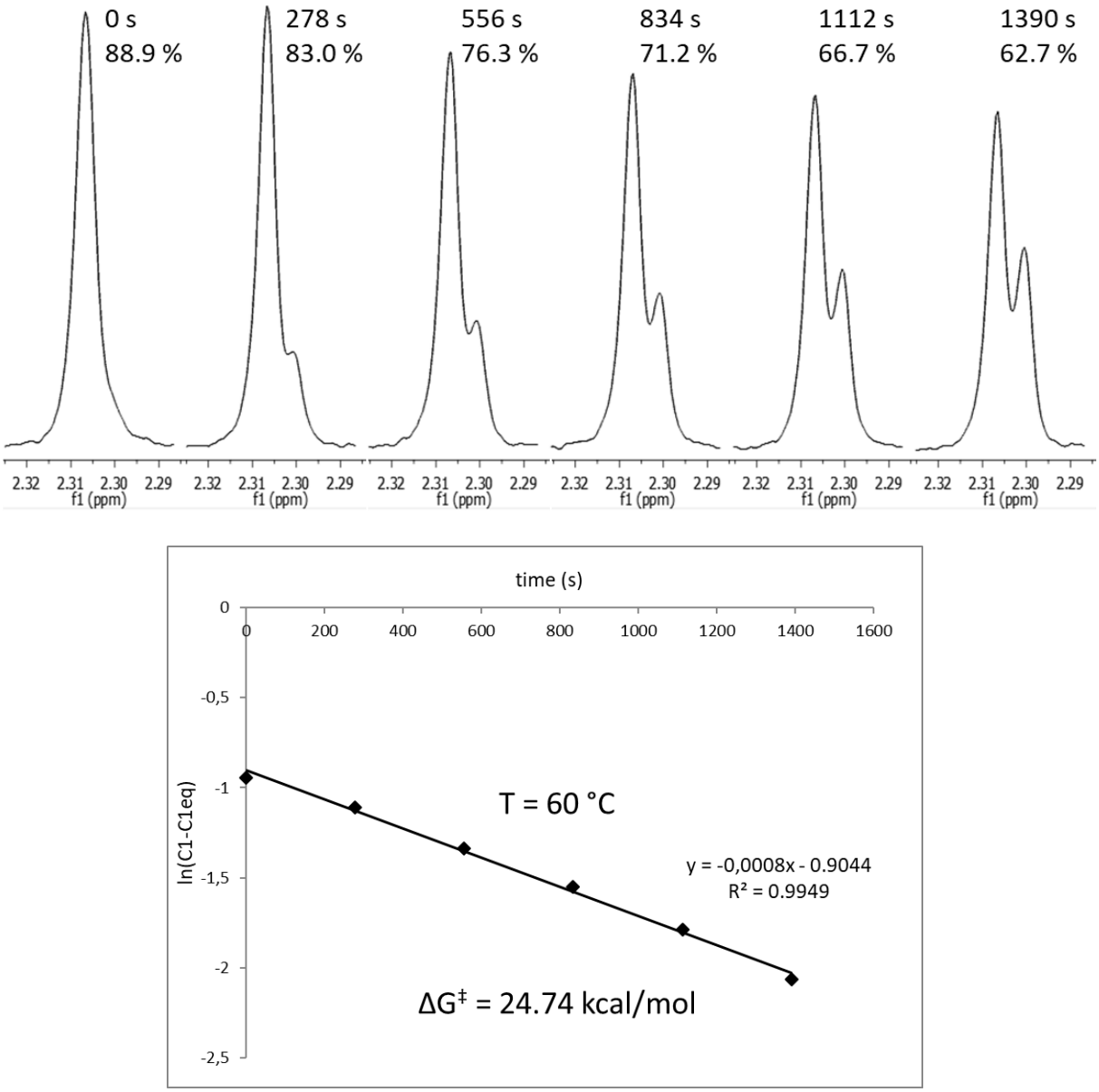

Figure 20: (above) NMR spectra of a sample of the second eluted peak of product **1** taken at intervals of 278 s, labelled with the time waited and the ratio between the heights of the chosen peaks expressed as a percentage. (below) A graph showing the linear regression of the results.

The NMR spectra of product **1** did not allow for proper integration of the peaks, so we measured the diastereomeric ratio by comparing the heights of the peaks.

Even though the HPLC spectrum of product **1** showed a diastereomeric ratio of around 60:40 (Figure 14a), calculations are made assuming an equilibrium ratio of 50:50, this is because we also made an NMR analysis of samples before and after a night spent at room temperature, which showed the equilibrium ratio to be very close to 50:50 (Figure 21).

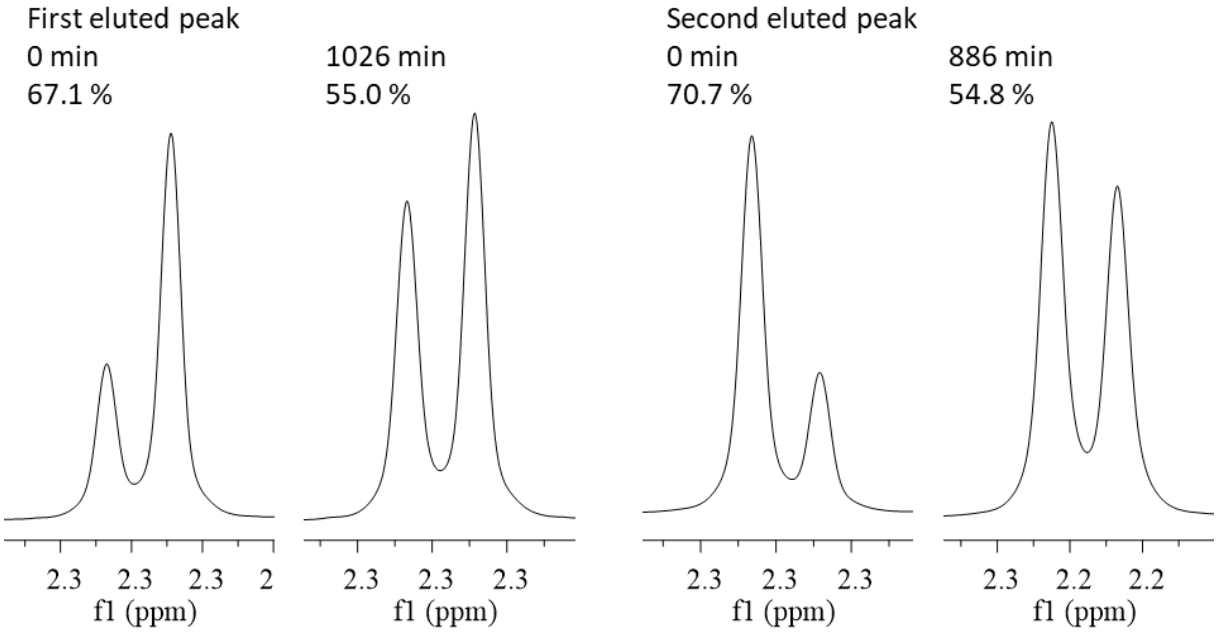

Figure 21: NMR spectra of a sample of the first eluted peak (left) and second eluted peak (right) of product **1** before and after a night spent at room temperature.

The NMR spectra of product 2 did not allow for proper integration either, so we again resorted to measuring the diastereomeric ratio by comparing the heights of the peaks. This likely caused inaccuracy in the results.

For the calculations we assumed an equilibrium ratio of 50:50, which is what is we saw from the HPLC analysis of the racemic mixture (Figure 14b).

The kinetic analysis of product 2 (Figures 22 and 23) resulted in an experimental energy barrier of 25.38 kcal/mol from the 3rd eluted peak and 24.89 kcal/mol from the 4th eluted peak, which are compatible with the previously calculated DFT value of 23.774 kcal/mol (Table 6).

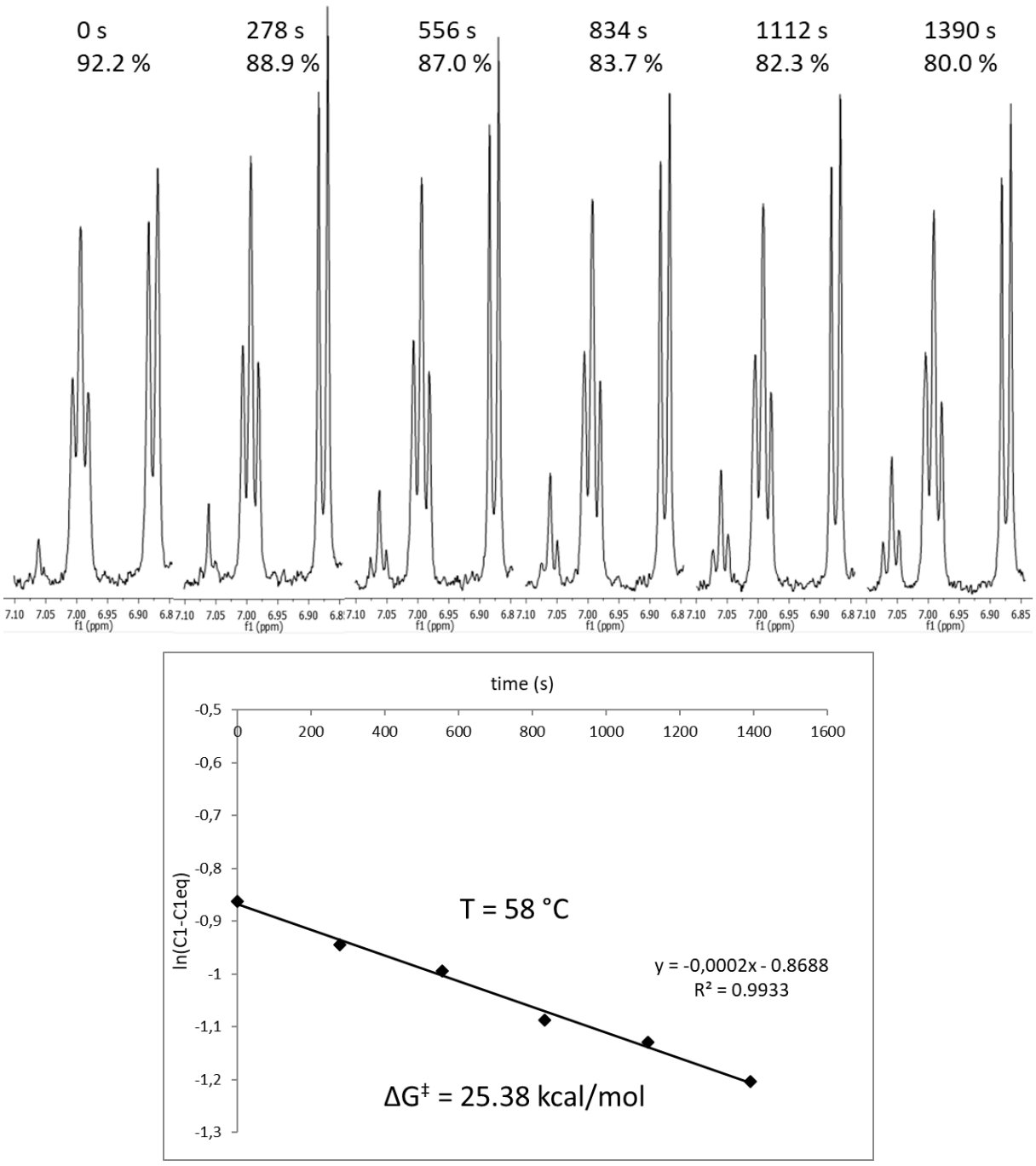

Figure 22: (above) NMR spectra of a sample of the third eluted peak of product **2** taken at intervals of 278 s, labelled with the time waited and the ratio between the heights of the chosen peaks expressed as a percentage. (below) A graph showing the linear regression of the results.

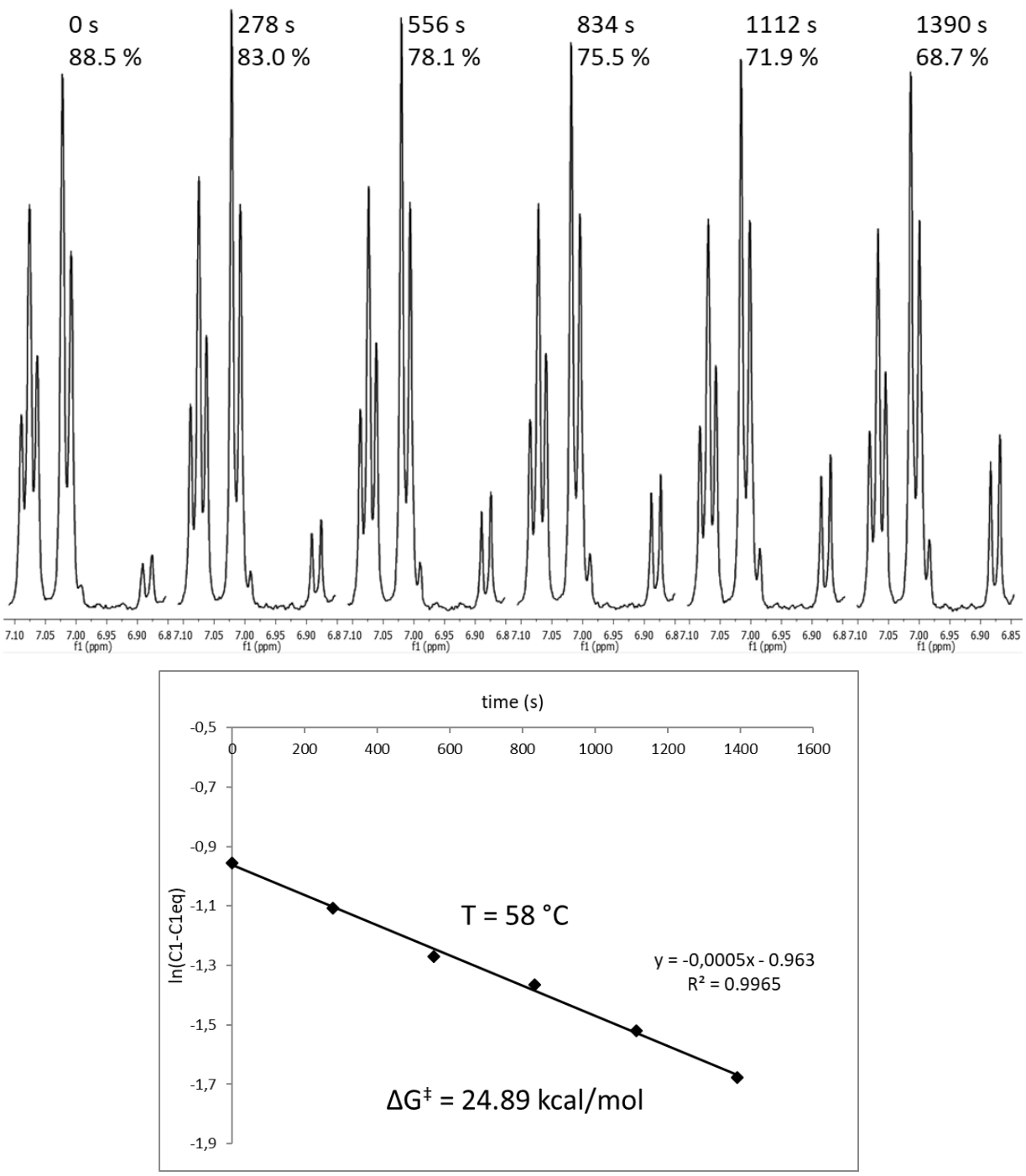

Figure 23: (above) NMR spectra of a sample of the fourth eluted peak of product **2** taken at intervals of 278 s, labelled with the time waited and the ratio between the heights of the chosen peaks expressed as a percentage. (below) A graph showing the linear regression of the results.

4. Conclusions:

4.1. Results:

We synthesized two fluorescent molecules and we successfully isolated the four stereoisomers of each through CSP-HPLC. We experimentally studied the kinetics behind the stereoisomerization of the two products and verified the computational predictions we made.
We confirmed the fluorescent properties of these molecules: under a 366 nm UV light, product **1** emits in a **bright blue** color while product **2** emits a **bright emerald green** (Figure 23).

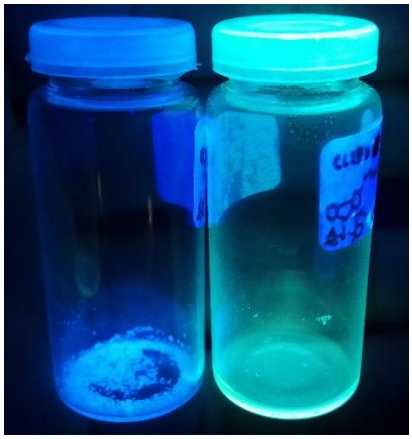

Figure 23: Photo of product **1** (left) and product **2** (right) under a 366 nm UV light.

This difference, caused by the electronic properties of the substituents on the carbazole, is consistent with our predictions.
This exhibited fluorescence does not seem to be quenched in the crystalline form, suggesting an AIE character.
ECD analysis has been used to assign the *M* configuration of the trifluoro-xylyl chiral axis to the 1st and 2nd eluted peak of compound **1**, and to the 1st and 4th eluted peak of compound **2**.
Our calculations predict a very strong TICT character and further analysis will be done on CPL.
All of these properties are promising and confirm the potential application of these molecules in fluorescent probes, non-linear optics and CP-OLEDs.

4.2. Future prospects:

Product **1** is of particular interest since it emits blue light, making it suitable to undergo further research in pursuit of cheap and efficient blue emitters for use in OLED screens and displays.

To move forward with this research, it will be imperative to synthesize a polymer and assess whether the photophysical properties are impaired by the presence of a polymer chain linked to the pendant emitter.

It is likely that a "spacer" between the emitter and the polymer will be needed, so different molecules will have to be synthetized and tested, since changing substituent on the carbazole will affect the emitter's properties.

The most important step in future research will be to produce an actual OLED device, to directly study the TADF character, AIE, internal efficiency and emission wavelength.

Lastly, the synthetic route should be optimized.

5. Experimental section:

5.1. Instrumentations:

Reactions which needed anhydrous conditions were performed under argon or nitrogen flow. The glassware used in these reactions was placed in an oven at +70 °C for at least 1 hour immediately before use.

^{1}H-NMR and ^{13}C-NMR spectra were registered with Varian Inova 600 MHz and Varian Mercury 400 MHz spectrometer. Chemical shifts are given in ppm relative to the internal standards tetramethylsilane or relative to the peak of the solvents. The deuterated solvents for NMR spectra were commercially available. Deuterated chloroform was filtered, before use, on aluminium oxide to remove HCl residues.

Silica gel 60 F254 (Merk) was employed for the TLC and silica gel 60 Å (230-400 mesh, Sigma Aldrich) was employed for flash chromatography separation of the reaction crudes.

HPLC Waters™ 600 instrument with detection fixed at 254 nm was used with chiral HPLC columns (CHIRALPAK® IB N-5 in different sizes and with different flow rates), a 95:5 mixture of *n*-hexane and chloroform was used as eluent for product **1** and an 85:15 mixture of *n*-hexane and chloroform was used as eluent for product **2**.

ECD spectra were obtained with JASCO J-810 spectropolarimeter at +25 °C in acetonitrile solution, using a quartz cell with 0.2 cm path length. The concentration of the sample was adjusted to reach about 1.0 in the maximum of absorbance. The spectrum was obtained from the average of 16 scans at 50 nm/min-1 scan rate.

5.2. Materials:

Cyclohexanone, 4-methoxyphenylhydrazine hydrochloride, Methacryloyl chloride, 2-bromo-1-methyl-3-(trifluoromethyl)benzene, potassium trifluoro(mesityl)-borate and 6-bromohexan-1-ol were commercially available.

THF has been dried before use by distillation from Na/benzophenone.

5.3. Calculations:

The calculations for ground states and transition states employed the B3LYP hybrid HF-DFT method and the 6-311G(d,p) basis sets. The analysis of the vibrational frequencies has shown no imaginary frequencies for ground states, and only one imaginary frequency for transition states. Transition states were also validated by visual inspection of their normal modes.

The fluorescence cycle was calculated using a procedure that has been optimized by the research group in a previous work, based on DFT and TD-DFT. This procedure involves 7 steps using the CAM-B3LYP functional.

1st step: a DFT geometry optimization on the ground state, considering the solute-solvent interaction, is done using the small 6-31G(d) basis set.

2nd step: three excited states are selected and a preliminary TD-DFT calculation, with the 6-31+G(d,p) basis set, identifies the transition at lowest energy.

3rd step: a DFT calculation, with the 6-31+G(d,p) basis set, accurately determines the ground state (S_0) energy and saves the solvation coordinates for use in the 4th step.

4th step: a TD-DFT calculation, with the 6-31+G(d,p) basis set and the solvation coordinates from the 3rd step, yields the vertical absorption energy.

5th step: a TD-DFT geometry optimization on the excited state (S_1), considering the solute-solvent interaction, is done using the small 6-31G(d) basis set.

6th step: a TD-DFT calculation, with the 6-31+G(d,p) basis set, determines the excited state (S_1) energy and saves the solvation coordinates for use in the 7th step.

7th step: a DFT calculation, with the 6-31+G(d,p) basis set and the solvation coordinates from the 6th step, yields the vertical emission energy.
The optimized geometries of the 1st and 5th steps are calculated once in THF, and then used as starting points in the same calculations for the other solvents.

The simulated ECD spectra were obtained with four different functionals (CAM-B3LYP, ωB97X-D, BH&HLYP and M06-2x) with the same 6-311++G(2d,p) basis set, this was done to have data redundancy and enhance reliability.

5.4. Synthesis and NMR characterization:

3-methoxy-9H-carbazole:

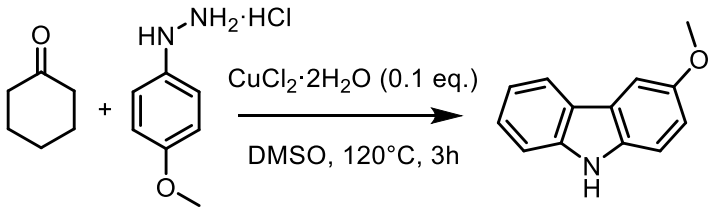

In a 25 mL oven-dried reaction flask, DMSO (5 mL), Cyclohexanone (236 µL), 4-methoxyphenylhydrazine hydrochloride (400 mg), and $CuCl_2 \cdot H_2O$ (38.9 mg) were added. The mixture was heated to 120°C and stirred for 3 h, leaving the flask open to allow oxygen from the air to enter. The solution was periodically checked with a TLC plate and after 2.5 h the spot corresponding to the intermediate disappeared. To remove the solvent, an extraction is performed using EtOAc and cold water. The organic phase contained a lot of water, so it was washed several times with brine and finally dehydrated with Na_2SO_4. The solvent was evaporated and the product was purified by flash column chromatography, with eluent petroleum ether and EtOAc in 92:8 ratio. Yield 63%.

^{1}H NMR (400 MHz, Chloroform-*d*) δ 8.08 (ddt, *J* = 7.9, 1.3, 0.7 Hz, 1H), 7.84 – 7.80 (m, 1H), 7.61 (d, *J* = 2.5 Hz, 1H), 7.48 – 7.39 (m, 1H), 7.34 (dt, *J* = 8.2, 0.8 Hz, 1H), 7.32 – 7.22 (m, 2H), 7.11 (dd, *J* = 8.7, 2.5 Hz, 1H), 3.97 (s, 3H).

9H-carbazol-3-ol:

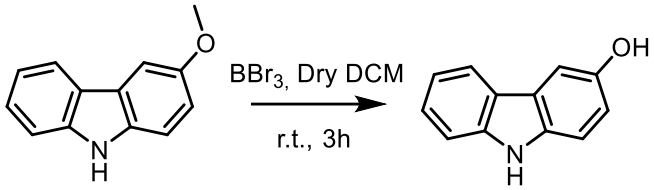

In a 50 mL oven-dried reaction flask, DCM (10 mL) and 3-methoxy-9H-carbazole (214 mg) were added. The solution was placed to cool in an ice bath, under nitrogen flow and stirred. BBr_3 1M (2.26 mL) was added slowly and in portions, then the solution was brought to room temperature to react. With a TLC plate, the substrate's absence is checked to assess whether the reaction is completed. The crude mixture was diluted with DCM and washed with water. The aqueous phase contained a lot of product, so it was washed with EtOAc. The two organic phases were washed with brine and dried with Na_2SO_4, to be then combined. The solvents were evaporated and the product was purified by flash column chromatography, with eluent petroleum ether and EtOAc in 3:1 ratio. Yield 92%.

^{1}H NMR (400 MHz, Chloroform-*d*) δ 7.99 (dd, *J* = 7.8, 0.9 Hz, 1H), 7.91 (s, 1H), 7.51 (dt, *J* = 2.6, 0.6 Hz, 1H), 7.43 – 7.37 (m, 2H), 7.30 (dd, *J* = 8.6, 0.6 Hz, 1H), 7.19 (ddd, *J* = 8.0, 4.8, 3.4 Hz, 1H), 6.98 (dd, *J* = 8.6, 2.5 Hz, 1H), 4.60 (s, 1H).

9H-carbazol-3-yl methacrylate:

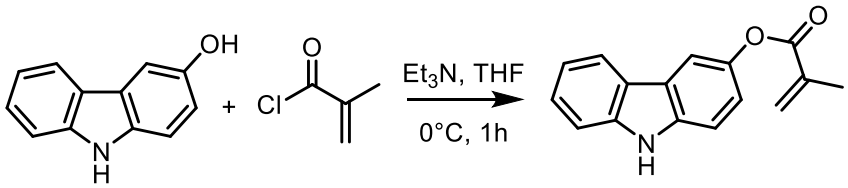

In a 50 mL oven-dried reaction flask, 9H-carbazol-3-ol (370 mg) and THF (anhydrous, distilled under nitrogen flow, 10 mL) were added. The solution was cooled in an ice bath and stirred under nitrogen flow. Et_3N (anhydrous, distilled under nitrogen flow, 280 µL) was added. Methacryloyl chloride (purified by distillation under nitrogen flow, 197 µL), diluted in THF (anhydrous, distilled under nitrogen flow, 5 mL) at 0°C, was then added dropwise. After 1 h the crude product is quickly filtered on Celite at 0°C, the filter was washed with EtOAc. The solvents were evaporated and the product was purified by flash column chromatography, with eluent petroleum ether and EtOAc in 6:1 ratio. Yield 73%.

^{1}H NMR (400 MHz, Chloroform-*d*) δ 8.08 (s, 1H), 8.00 (dq, *J* = 7.9, 0.9 Hz, 1H), 7.81 (dt, *J* = 2.3, 0.6 Hz, 1H), 7.44 – 7.41 (m, 2H), 7.40 (dd, *J* = 8.6, 0.6 Hz, 1H), 7.25 – 7.19 (m, 1H), 7.16 (dd, *J* = 8.7, 2.3 Hz, 1H), 6.41 (dq, *J* = 1.9, 1.0 Hz, 1H), 5.78 (p, *J* = 1.5 Hz, 1H), 2.12 (dd, *J* = 1.6, 1.0 Hz, 3H).

Product **1**, **9-(mesityl(2-methyl-6-(trifluoromethyl)phenyl)boraneyl)-9H-carbazol-3-yl methacrylate**:

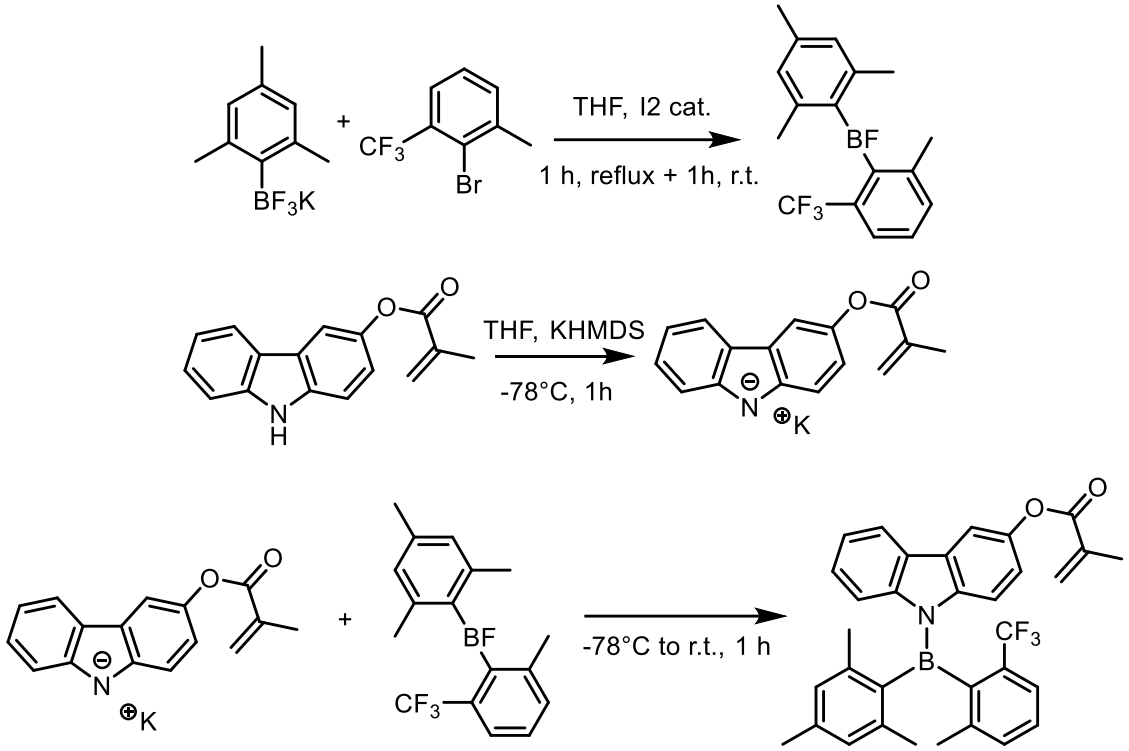

In a 15 mL oven-dried reaction flask under argon flow, Mg turnings (cleaned with HCl 1M, isopropanol and anhydrous THF, 103 mg), 2-bromo-1-methyl-3-(trifluoromethyl)benzene (66.3 µL), THF (anhydrous, distilled under nitrogen flow, 4 mL) and a tip of I_2 were added at room temperature. The mixture was stirred and heated to reflux. After 10 min a color change occurs, from that point the reaction is left to react for 1 h. It is then cooled to room temperature, potassium trifluoro(mesityl)-borate (96.5 mg) was added and the mixture was stirred for another hour. During this time, in a second 15 mL oven-dried reaction flask under argon flow, 9H-carbazol-3-yl methacrylate (107 mg), THF (anhydrous, distilled under nitrogen flow, 4 mL) and KHMDS (0.5 M, 0.854 mL) were added at -78°C. This reaction is considered complete after 30 min. When the first reaction is complete, it is cooled to -78°C and transported dropwise into the second flask. The mixture is left to warm up slowly to room temperature for 1 h. It is then quenched with DCM, filtered on Celite and purified by flash column chromatography, with eluent petroleum ether and EtOAc in 97.5:2.5 ratio. Yield 45%.

^{1}H NMR (600 MHz, Chloroform-*d*) δ 7.93 – 7.89 (m, 1H), 7.73 (t, *J* = 2.4 Hz, 1H), 7.60 (t, *J* = 7.0 Hz, 1H), 7.46 (td, *J* = 7.8, 5.3 Hz, 1H), 7.33 – 7.27 (m, 1H), 7.25 – 7.21 (m, 1H), 7.12 (ddd, *J* = 8.5, 7.2, 1.3 Hz, 1H), 7.07 – 7.03 (m, 1H), 7.00 (d, *J* = 9.0 Hz, 1H), 6.87 – 6.77 (m, 3H), 6.36 (dt, *J* = 7.8, 1.2 Hz, 1H), 5.76 (ddp, *J* = 4.7, 3.1, 1.6 Hz, 1H), 2.32 (d, *J* = 5.4 Hz, 3H), 2.08 (dt, *J* = 6.8, 1.2 Hz, 3H), 1.99 (s, 6H), 1.90 (s, 3H).

^{19}F NMR (376 MHz, Chloroform-*d*) δ -57.29.

^{1}H NMR 600 MHz Chloroform-*d* (product **1**):

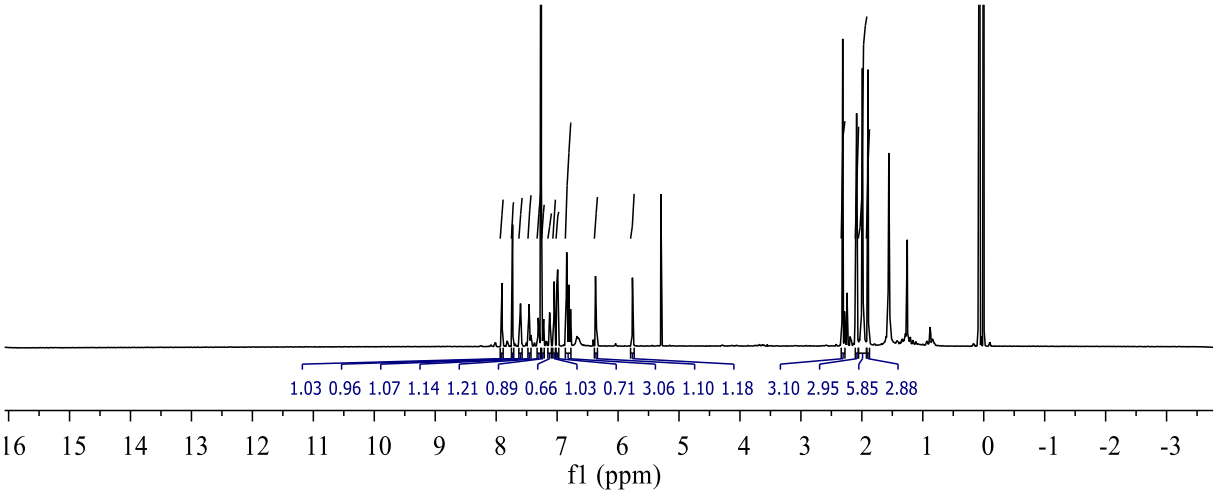

Zoom aromatic ^{1}H NMR (product **1**):

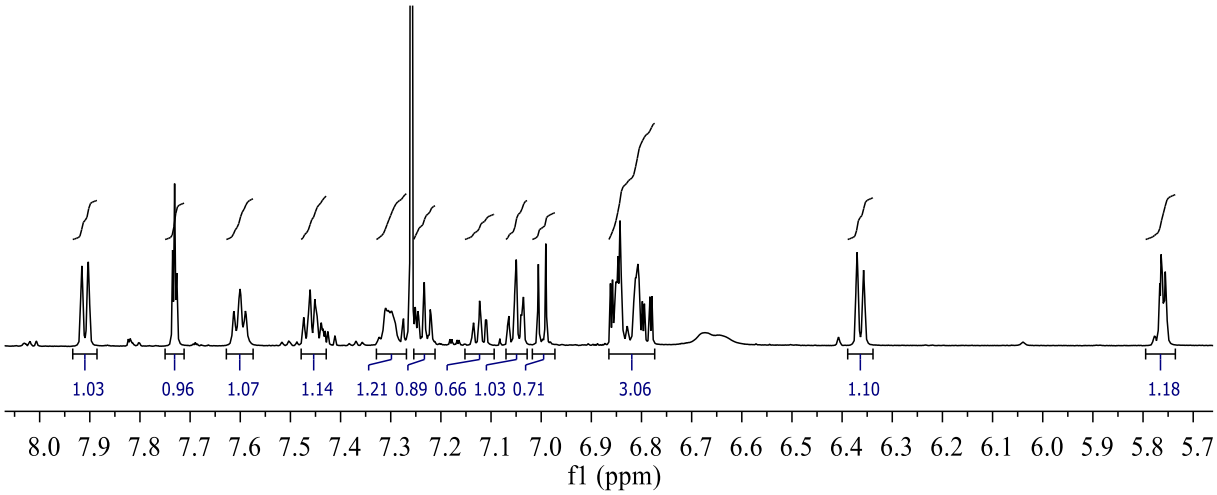

6-((9H-carbazol-3-yl)oxy)hexan-1-ol:

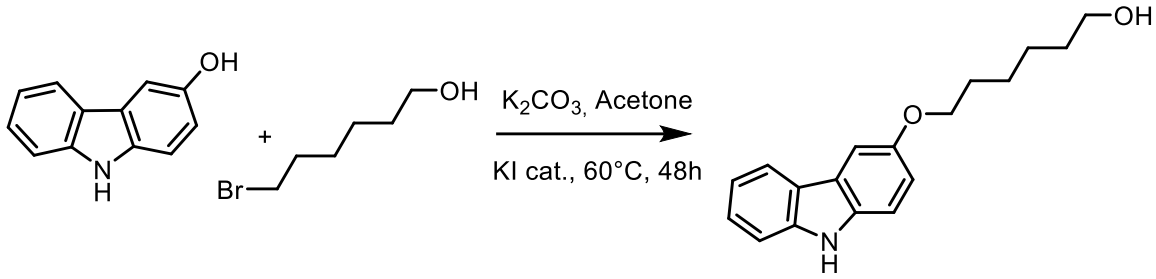

In a 25 mL oven-dried reaction flask, 9H-carbazol-3-ol (170 mg), acetone (7 mL), K_2CO_3 (218 mg), a crystal of KI and 6-bromohexan-1-ol (146 µL) were added. The solution was heated to 120°C under nitrogen flow and stirred for 48 h (the reaction was still not complete). The crude mixture was filtered on Celite, the solvents were evaporated and the product was purified by flash column chromatography, with eluent petroleum ether and EtOAc in 2:1 ratio. Yield 57%.

^{1}H NMR (400 MHz, Chloroform-*d*) δ 8.02 (dq, *J* = 7.8, 0.9 Hz, 1H), 7.91 (s, 1H), 7.55 (d, *J* = 2.5 Hz, 1H), 7.43 – 7.36 (m, 2H), 7.32 (dd, *J* = 8.8, 0.6 Hz, 1H), 7.20 (ddd, *J* = 8.1, 5.5, 2.6 Hz, 1H), 7.06 (dd, *J* = 8.7, 2.5 Hz, 1H), 4.08 (t, *J* = 6.5 Hz, 2H), 3.68 (t, *J* = 6.5 Hz, 2H), 1.86 (dt, *J* = 14.5, 6.6 Hz, 2H), 1.69 – 1.58 (m, 3H), 1.54 – 1.43 (m, 3H), 1.25 (s, 1H).

6-((9H-carbazol-3-yl)oxy)hexyl methacrylate:

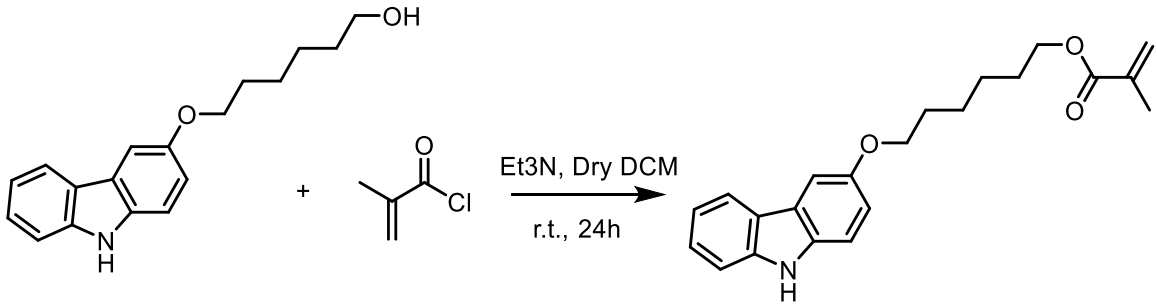

In a 50 mL oven-dried reaction flask, 6-((9H-carbazol-3-yl)oxy)hexan-1-ol (155 mg) and DCM (10 mL) were added. The solution was cooled in an ice bath and stirred under nitrogen flow. Et_3N (anhydrous, distilled under nitrogen flow, 91 µL) was added. Methacryloyl chloride (purified by distillation under nitrogen flow, 64 µL), diluted in DCM (5 mL) at 0°C, was then added dropwise. After 24 h the crude product is quickly filtered on Celite at 0°C, the filter was washed with EtOAc. The solvents were evaporated and the product was purified by flash column chromatography, with eluent petroleum ether and EtOAc in 6:1 ratio. Yield 86%.

^{1}H NMR (400 MHz, Chloroform-*d*) δ 8.08 – 8.01 (m, 2H), 7.58 (d, *J* = 2.5 Hz, 1H), 7.46 – 7.32 (m, 2H), 7.28 – 7.17 (m, 2H), 7.07 (dd, *J* = 8.7, 2.5 Hz, 1H), 6.14 (dq, *J* = 1.9, 1.0 Hz, 1H), 5.57 (h, *J* = 1.5 Hz, 1H), 4.24 – 4.14 (m, 2H), 4.08 (t, *J* = 6.5 Hz, 2H), 1.98 (dd, *J* = 1.6, 1.0 Hz, 3H), 1.91 – 1.82 (m, 2H), 1.79 – 1.69 (m, 2H), 1.63 – 1.55 (m, 2H), 1.54 – 1.44 (m, 2H).

Product **2**, **6-((9-(mesityl(2-methyl-6-(trifluoromethyl)phenyl)boraneyl)-9H-carbazol-3-yl)oxy)hexyl methacrylate**:

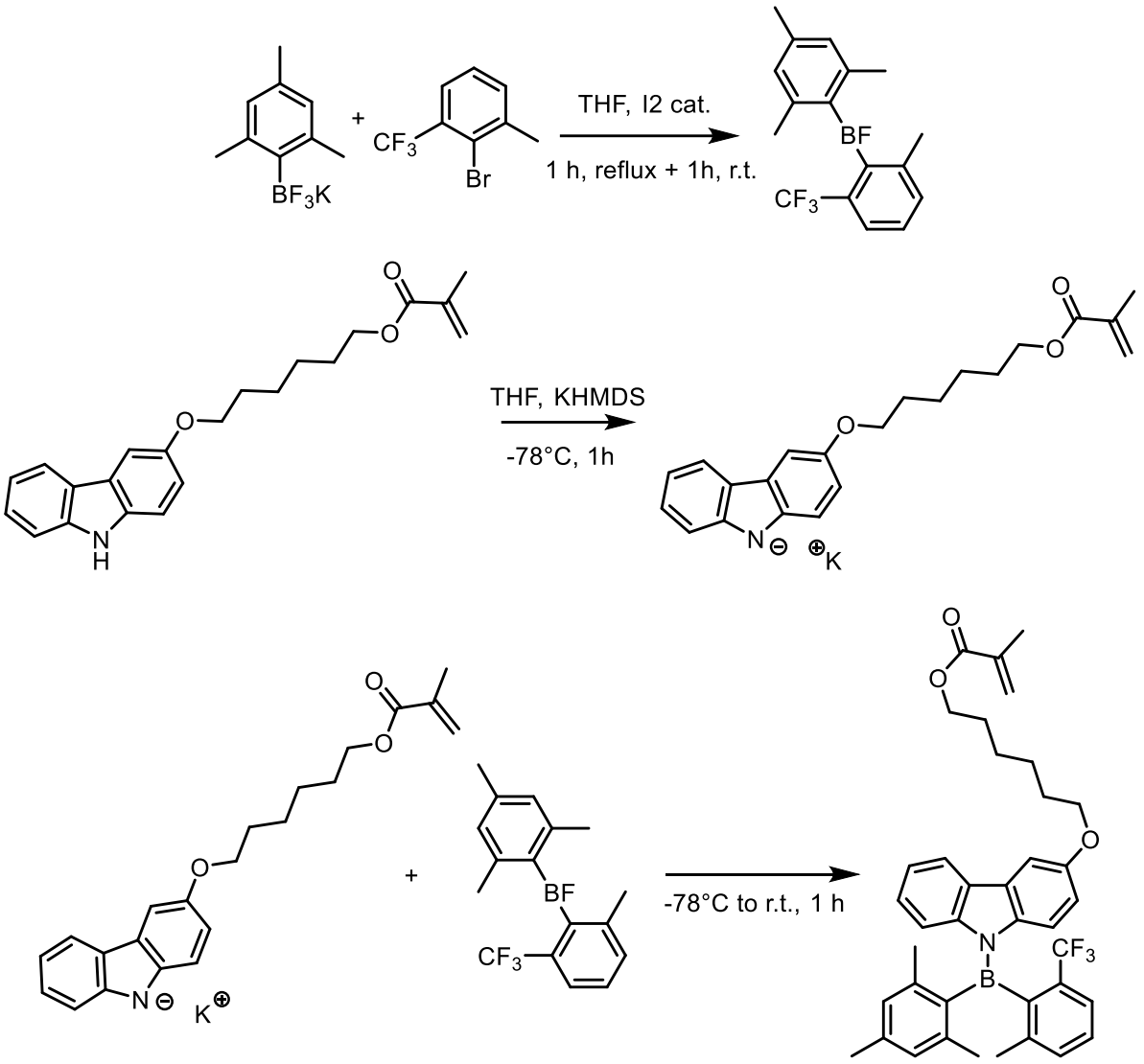

In a 15 mL oven-dried reaction flask under argon flow, Mg turnings (cleaned with HCl 1M, isopropanol and anhydrous THF, 113 mg), 2-bromo-1-methyl-3-(trifluoromethyl)benzene (72 µL), THF (anhydrous, distilled under nitrogen flow, 5 mL) and a tip of I_2 were added at room temperature. The mixture was stirred and heated to reflux. After 10 min a color change occurs, from that point the reaction is left to react for 1 h. It is then cooled to room temperature, potassium trifluoro(mesityl)-borate (105 mg) was added and the mixture was stirred for another hour. During this time, in a second 15 mL oven-dried reaction flask under argon flow, 6-((9H-carbazol-3-yl)oxy)hexyl methacrylate (163 mg), THF (anhydrous, distilled under nitrogen flow, 5 mL) and KHMDS (0.5 M, 0.926 mL) were added at -78°C. This reaction is considered complete after 30 min.

When the first reaction is complete, it is cooled to -78°C and transported dropwise into the second flask. The mixture is left to warm up slowly to room temperature for 1 h. It is then quenched with DCM, filtered on Celite and purified by flash column chromatography, with eluent petroleum ether and EtOAc in 96:4 ratio. Yield 58%.

^{1}H NMR (400 MHz, Chloroform-*d*) δ 7.94 (dq, *J* = 7.7, 1.1 Hz, 1H), 7.62 (d, *J* = 7.8 Hz, 1H), 7.50 – 7.41 (m, 2H), 7.34 – 7.29 (m, 1H), 7.28 – 7.21 (m, 1H), 7.15 – 6.91 (m, 2H), 6.90 – 6.81 (m, 2H), 6.70 (ddd, *J* = 26.5, 9.1, 2.6 Hz, 2H), 6.13 (tq, *J* = 2.0, 1.0 Hz, 1H), 5.55 (hept, *J* = 1.6 Hz, 1H), 4.19 (td, *J* = 6.6, 2.7 Hz, 2H), 4.05 (dt, *J* = 7.6, 6.4 Hz, 2H), 2.34 (s, 3H), 2.04 (dd, *J* = 10.9, 8.3 Hz, 6H), 1.96 (td, *J* = 1.6, 1.0 Hz, 3H), 1.93 (s, 3H), 1.90 – 1.69 (m, 4H), 1.64 – 1.43 (m, 4H).

^{19}F NMR (376 MHz, Chloroform-*d*) δ -57.35.

^{1}H NMR 600 MHz Chloroform-*d* (product **2**):

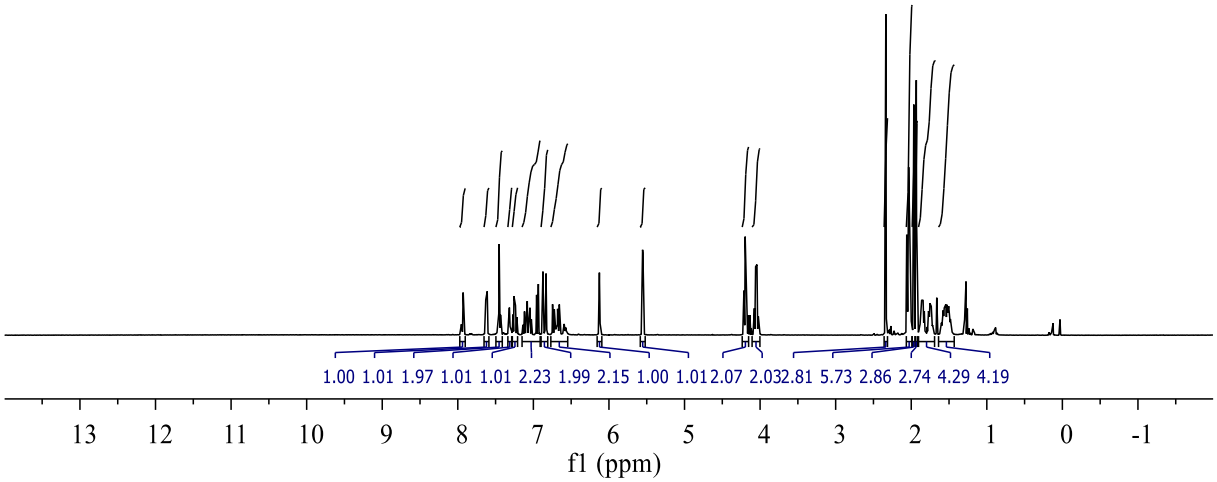

Zoom aromatic ^{1}H NMR (product **2**):

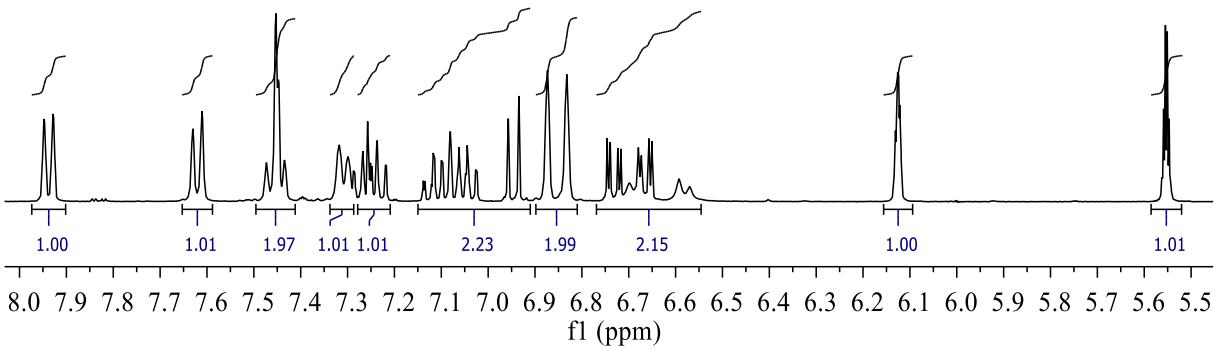

6. Bibliography:

[1] Yam, F. K., and Zainuriah Hassan. "Innovative advances in LED technology." *Microelectronics Journal* **2005**, *36*, 129-137. doi.org/10.1016/j.mejo.2004.11.008

[2] Salehi, Amin, et al. "Recent advances in OLED optical design." *Advanced Functional Materials* **2019**, *29*, 1808803. doi.org/10.1002/adfm.201808803

[3] Hai, Nie, Zhang Bo, and Tang Xian-Zhong. "Significant improvement of OLED efficiency and stability by doping both HTL and ETL with different dopant in heterojunction of polymer/small-molecules." *Chinese Physics* **2007**, *16*, 730. doi.org/10.1088/1009-1963/16/3/028

[4] Wang, Jianpu, et al. "Control of exciton spin statistics through spin polarization in organic optoelectronic devices." *Nature communications* **2012**, *3*, 1-6. doi.org/10.1038/ncomms2194

[5] Partee, J., et al. "Delayed fluorescence and triplet-triplet annihilation in π-conjugated polymers." *Physical review letters* **1999**, *82*, 3673. doi.org/10.1103/PhysRevLett.82.3673

[6] Huang, Tianyu, Wei Jiang, and Lian Duan. "Recent progress in solution processable TADF materials for organic light-emitting diodes." *Journal of Materials Chemistry C* **2018**, *6*, 5577-5596. doi.org/10.1039/C8TC01139G

[7] Nayak, Debashish, and Ram Bilash Choudhary. 'Conducting Polymer-Based Emissive Layer on Efficiency of OLEDs'. Light-Emitting Diodes and Photodetectors - Advances and Future Directions [Working Title], IntechOpen, June **2021**. doi.org/10.5772/intechopen.98652

[8] Teng, Jin-Ming, Yin-Feng Wang, and Chuan-Feng Chen. "Recent progress of narrowband TADF emitters and their applications in OLEDs." *Journal of Materials Chemistry C* **2020**, *8*, 11340-11353. doi.org/10.1039/D0TC02682D

[9] Abroshan, Hadi, Veaceslav Coropceanu, and Jean-Luc Brédas. "Hyperfluorescence-based emission in purely organic materials: Suppression of energy-loss mechanisms via alignment of triplet excited states." *ACS Materials Letters* **2020**, *2*, 1412-1418. doi.org/10.1021/acsmaterialslett.0c00407

[10] Kirch, Anton, Max Gmelch, and Sebastian Reineke. "Simultaneous Singlet–Singlet and Triplet–Singlet Förster Resonance Energy Transfer from a Single Donor Material." *The journal of physical chemistry letters* **2019**, *10*, 310-315. doi.org/10.1021/acs.jpclett.8b03668

[11] Borchardt, John K. "Developments in organic displays." *Materials Today* **2004**, *7*, 42-46. doi.org/10.1016/S1369-7021(04)00401-8

[12] Hong, Yuning, Jacky WY Lam, and Ben Zhong Tang. "Aggregation-induced emission." *Chemical Society Reviews* **2011**, *40*, 5361-5388. doi.org/10.1039/C1CS15113D

[13] Yu, Maoxing, et al. "Promising applications of aggregation-induced emission luminogens in organic optoelectronic devices." *PhotoniX* **2020**, *1*, 1-33. doi.org/10.1186/s43074-020-00012-y

[14] Lee, Sebok, et al. "Twisted intramolecular charge transfer of nitroaromatic push–pull chromophores." *Scientific Reports* **2022**, *12*, 6557. doi.org/10.1038/s41598-022-10565-6

[15] Wang, Jian, et al. "Substituent effects on twisted internal charge transfer excited states of N-borylated carbazoles and (diphenylamino) boranes." *The Journal of Physical Chemistry A* **2012**, *116*, 1151-1158. doi.org/10.1021/jp209264j

[16] Hu, Rongrong, et al. "Twisted intramolecular charge transfer and aggregation-induced emission of BODIPY derivatives." *The Journal of Physical Chemistry C* **2009**, *113*, 15845-15853. doi.org/10.1021/jp902962h

[17] Pescitelli, Gennaro. "Electronic Circular Dichroism." *Encyclopedia*. Web. 14 June, **2019.**

[18] Wan, Li, et al. "Inverting the handedness of circularly polarized luminescence from light-emitting polymers using film thickness." *ACS nano* **2019**, *13*, 8099-8105. doi.org/10.1021/acsnano.9b02940

[19] Singh, Ranbir, KN Narayanan Unni, and Ankur Solanki. "Improving the contrast ratio of OLED displays: An analysis of various techniques." *Optical Materials* **2012**, *34*, 716-723. doi.org/10.1016/j.optmat.2011.10.005

[20] Kim, Bong Choon, et al. "Wideband antireflective circular polarizer exhibiting a perfect dark state in organic light-emitting-diode display." *Optics Express* **2014**, *22*, A1725-A1730. doi.org/10.1364/OE.22.0A1725

[21] Ma, Xin-Li, et al. "P-126: A New Coatable Circular Polarizer for Anti-Reflection of Flexible AMOLED." *SID Symposium Digest of Technical Papers*. **2017**, *48*, 1735-1737 doi.org/10.1002/sdtp.11998

[22] Brandt, Jochen R., et al. "Circularly polarized phosphorescent electroluminescence with a high dissymmetry factor from PHOLEDs based on a platinahelicene." *Journal of the American Chemical Society* **2016**, *138*, 9743-9746. doi.org/10.1021/jacs.6b02463

[23] LaPlante, Steven R., et al. "Assessing atropisomer axial chirality in drug discovery and development." *Journal of medicinal chemistry* **2011**, *54*, 7005-7022. doi.org/10.1021/jm200584g

[24] Liu, Qin-De, et al. "From blue to red: syntheses, structures, electronic and electroluminescent properties of tunable luminescent N, N chelate boron complexes." *Advanced Functional Materials* **2005**, *15*, 143-154. doi.org/10.1002/adfm.200400081

[25] Li, Hai-Jun, et al. "D− π–A Triarylboranes as Reversible Fluorescent Probes for CO2 and Temperature." *Organic letters* **2019**, *21*, 2838-2842. doi.org/10.1021/acs.orglett.9b00831

[26] Alam, Md Mehboob, Mausumi Chattopadhyaya, and Swapan Chakrabarti. "A critical theoretical study on the two-photon absorption properties of some selective triaryl borane-1-naphthylphenyl amine based charge transfer molecules." *Physical Chemistry Chemical Physics* **2011**, *13*, 9285-9292. doi.org/10.1039/C0CP02958K

[27] Shi, Yong-gang, et al. "A simple multi-responsive system based on aldehyde functionalized amino-boranes." *Chemical science* **2018**, *9*, 1902-1911. doi.org/10.1039/C7SC03617E

[28] Ganesan, Paramaguru, et al. "Methoxy substituents activated carbazole-based boron dimesityl TADF emitters." *Journal of Materials Chemistry C* **2020**, *8*, 4780-4788. doi.org/10.1039/C9TC07020F

[29] Waszkowska, Karolina, et al. "Correlation between Nonlinear Optical Effects and Structural Features of Aurone-Based Methacrylic Polymeric Thin Films." *Materials* **2022**, *15*, 6076 doi.org/10.3390/ma15176076

[30] Sasaki, Shunsuke, Gregor PC Drummen, and Gen-ichi Konishi. "Recent advances in twisted intramolecular charge transfer (TICT) fluorescence and related phenomena in materials chemistry." *Journal of Materials Chemistry C* **2016**, *4*, 2731-2743. doi.org/10.1039/C5TC03933A

[31] Arivazhagan, C., et al. "Phenothiazinyl boranes: a new class of AIE luminogens with mega Stokes shift, mechanochromism, and mechanoluminescence." *Chemistry–A European Journal* **2017**, *23*, 7046-7051. doi.org/10.1002/chem.201700187

[32] Gebeyehu, D., et al. "Highly efficient deep-blue organic light-emitting diodes with doped transport layers." *Synthetic metals* **2005**, *148*, 205-211. doi.org/10.1016/j.synthmet.2004.09.024

[33] Mislow, Kurt. "Stereochemical consequences of correlated rotation in molecular propellers." *Accounts of Chemical Research* **1976**, *9*, 26-33.

[34] Pecorari, Daniel, et al. "Highly twisted carbazole-borane derivatives: B–N stereodynamic analysis and consequences on their emission properties." *Organic Chemistry Frontiers* **2021**, *8*, 4496-4507. doi.org/10.1039/D1QO00715G